Research Square

Preprints are preliminary reports that have not undergone peer review.
They should not be considered conclusive, used to inform clinical practice,
or referenced by the media as validated information.

Fabrication of an acid-treated 3D-printed Perlite monolithic adsorbent for efficient removal of organic dyes from aqueous solution

Fatemeh Ranjbar
Iran Polymer and Petrochemical Institute
Amir Masood Rezadoust
Iran Polymer and Petrochemical Institute
Samahe Sadjadi
s.sadjadi@ippi.ac.ir

Iran Polymer and Petrochemical Institute

Research Article

Keywords: 3D-printing, Perlite, Acid treatment, Adsorbent, Water treatment

Posted Date: November 16th, 2026

DOI: https://doi.org/10.21203/rs.3.rs-11518403/v1

License: This work is licensed under a Creative Commons Attribution 4.0 International License.
Read Full License

Additional Declarations: No competing interests reported.

Fabrication of an acid-treated 3D-printed Perlite monolithic adsorbent for efficient removal of organic dyes from aqueous solution

Abstract

Three-dimensional Perlite-based monolithic adsorbents with different Perlite loadings (3D-Per5, 3D-Per10, and 3D-Per15) were fabricated via digital light processing (DLP) 3D printing for methylene blue (MB) removal from aqueous solutions. The influence of Perlite loading on adsorption performance was systematically investigated, with 3D-Per15 exhibiting the highest adsorption capacity. To further improve its performance, the optimized monolith was subjected to acid treatment, which removed surface impurities, increased the exposure of accessible adsorption sites, and enhanced pore accessibility, thereby significantly promoting dye adsorption while preserving the structural integrity of the printed monolith. The adsorption behavior was evaluated under different operating conditions. The highest MB removal efficiency of 89% and a maximum adsorption capacity of 17.8 mg g^{-1} were achieved at pH=10 and 85 °C after 100 min. Kinetic analysis yielded an activation energy of 27.14 kJ mol^{-1}, while thermodynamic parameters confirmed that the adsorption process was endothermic (ΔH = 24.36 kJ mol^{-1}) with a negative entropy change ($\Delta S = -179.91$ J mol^{-1} K^{-1}). These findings demonstrate that integrating DLP 3D printing with post-print acid activation is a simple and effective strategy for developing high-performance monolithic adsorbents for wastewater treatment.

Keywords: 3D-printing; Perlite; Acid treatment; Adsorbent; Water treatment

1. Introduction

The rapid growth of industrial activities has led to the continuous discharge of large quantities of dye-containing effluents into aquatic environments [1-6]. Among various organic pollutants, synthetic dyes are considered one of the most problematic contaminants due to their complex

molecular structures, high stability, resistance to biodegradation, and potential toxicity to living organisms[7-9]. Methylene blue (MB), a cationic dye extensively used in textile, paper, printing, and pharmaceutical industries, is frequently detected in industrial wastewater [10; 11]. The presence of MB in water bodies not only deteriorates water quality and aesthetic appearance but also reduces light penetration, disrupts aquatic ecosystems, and may pose adverse effects on human health [12]. Consequently, the development of efficient and sustainable technologies for dye removal has become an important research priority in the field of environmental remediation [13; 14].

Various treatment technologies, including adsorption [15; 16], ion exchange [17], coagulation [16], membrane filtration [18], advanced oxidation processes [19], biological degradation [20], and photocatalysis [21], have been explored for the elimination of dye pollutants from wastewater [22-24]. However, many of these approaches suffer from limitations such as high operational costs, complicated processing steps, generation of secondary pollutants, or limited efficiency towards highly stable dye molecules [25-27]. In contrast, adsorption has emerged as one of the most attractive treatment methods owing to its simplicity, high removal efficiency, operational flexibility, and economic feasibility [28; 29]. The effectiveness of adsorption processes strongly depends on the physicochemical properties of the adsorbent, motivating extensive efforts [30; 31] toward the development of novel adsorptive materials with enhanced performance [29; 32]. Natural mineral-based adsorbents have attracted increasing attention as low-cost and environmentally benign alternatives to conventional adsorbents [33-35]. Among them, Perlite has received considerable interest due to its abundance, low density, chemical stability, non-toxicity, and porous structure [36-38]. Perlite is a naturally occurring volcanic aluminosilicate material that can provide accessible adsorption sites for the uptake of various contaminants. Previous studies have demonstrated the potential of Perlite for the removal of dyes, heavy metals, and other pollutants from aqueous solutions [39; 40].

Despite the remarkable adsorption performance achieved by many powdered adsorbents, their practical application is often challenged by difficult recovery [41] and reusability after treatment [42]. Separation of fine particles from treated water generally requires additional filtration or centrifugation steps, increasing process complexity and operational costs [43]. In recent years, three-dimensional (3D) printing technology has emerged as an innovative manufacturing approach capable of overcoming these limitations. By enabling the fabrication of monolithic structures with controlled geometry, porosity, and architecture, 3D printing offers new opportunities for designing adsorbents with improved handling characteristics and facile recovery from aqueous media [44]. Among different additive manufacturing techniques, digital light processing (DLP) has gained particular attention due to its high printing resolution, rapid fabrication speed, and ability to produce complex structures with excellent dimensional accuracy [45-47]. DLP technology enables precise control over structural features [48-50] that directly influence mass transfer behavior and adsorption performance [51-54]. Consequently, DLP-fabricated adsorbents have recently attracted significant interest for environmental applications, especially in water purification and wastewater treatment processes [55]. Although DLP printing enables the fabrication of monolithic adsorbents with well-defined architectures and excellent recoverability, their adsorption performance is still largely governed by the physicochemical characteristics of the exposed surface. Therefore, surface modification has attracted increasing attention as an effective strategy to further improve the adsorption efficiency of printed monoliths [56]. Among different modification methods, acid treatment has proven particularly effective because it can remove surface impurities, increase surface roughness, improve pore accessibility, and expose additional active adsorption sites without altering the overall printed geometry [21]. Such structural and chemical modifications may significantly improve adsorption efficiency and strengthen interactions between adsorbent surfaces and dye molecules [57; 58].

Although considerable progress has been achieved in the development of 3D-printed adsorbents, studies focusing on Perlite-based monolithic structures have remained limited. Furthermore, the combined effects of Perlite incorporation, structural design through DLP printing, and post-fabrication acid treatment on dye adsorption performance have not been comprehensively investigated. Addressing these challenges may contribute to the development of efficient, recoverable, and economically attractive adsorbents for practical wastewater treatment applications. Accordingly, the present work aims to fabricate a series of Perlite-based three-dimensional adsorbents, designated as 3D-Per5, 3D-Per10, and 3D-Per15, using digital light processing (DLP) 3D printing technology. The influence of Perlite loading on the adsorption performance was systematically evaluated to identify the optimum composition. Subsequently, the best-performing monolithic adsorbent was subjected to a post-printing acid-washing treatment as a key surface activation step. The adsorption behavior toward methylene blue was investigated under different operating conditions, and kinetic and thermodynamic analyses were performed to elucidate the adsorption mechanism and evaluate the potential of the developed acid-activated monolithic adsorbents for wastewater remediation.

2. Experimental

2.1.Reagents

Raw Perlite was provided by a local mineral company. Ethanol (EtOH, >99%), sulfuric acid (H_2SO_4 > 96%), Methyl Orange (MO), Methylene Blue (MB), Congo Red (CR), and Rhodamine B (RhB) were obtained from Sigma-Aldrich (Germany). These dyes were employed as model organic pollutants to assess the adsorption performance of the fabricated 3D-printed adsorbents. The 3D-Perlite5, 3D-Perlite10, 3D-Perlite15 were fabricated using a digital light processing (DLP) and an ABS-like Pro resin (acrylate-based UV-curable resin) purchased from Anycubic (China).

2.2.Instruments

Various characterization techniques were employed to investigate the properties of the 3D-printed adsorbent. Surface morphology and elemental composition were analyzed using scanning electron microscopy (SEM, VEGA II TESCAN, Czech Republic) coupled with energy-dispersive X-ray spectroscopy (EDS, QX2, RONTEC). Fourier-transform infrared spectroscopy (FT-IR, using KBr pellets) and X-ray diffraction (XRD, Rigaku Ultima IV with Cu-Kα radiation) were used to study the structural characteristics of the samples. Thermal stability was evaluated by thermogravimetric analysis (TGA, METTLER TOLEDO) under an O_2 atmosphere at a heating rate of 10 °C min^{-1}. Mechanical properties were assessed through compression testing using a universal testing machine (STM20, Santam) according to the ISO 604 standard. The concentration of dye solutions after adsorption was determined using a UV–Vis spectrophotometer (Shimadzu, Model 1700). In addition, the specific surface area of the adsorbents was determined using the Brunauer–Emmett–Teller (BET) method (BELSORP Mini II instrument). The samples were degassed at 110 ˚C for 2h to remove physically adsorbed moisture.

2.3.Ink preparation

To prepare the printing ink for the manufacturing of Perlite-containing monoliths, ABS-like Pro resin (20 g) was mixed with different amounts of Perlite, i.e. 1, 2 and 3 g, to obtain samples Per5, Per10 and Per15, respectively. It is worth noting that one of the major challenges associated with the fabrication of particle-loaded 3D-printed composites is the gradual sedimentation of solid particles during the printing process, which may result in non-uniform particle distribution throughout the printed construct. Such heterogeneity can adversely affect the reproducibility and efficiency of the adsorption process. Therefore, appropriate homogenization of the printing suspension prior to fabrication, together with optimization of

the printing parameters and structural design, is essential to ensure uniform distribution of Perlite particles and consistent adsorption performance in the resulting monolith. For this reason, the resulting mixture was then subjected to ultrasonic irradiation (at 140 W) for 10 min to obtain a uniform composition. It is worth noting that the numbers assigned to the samples indicate the mass fraction of Perlite in the printing ink formulation.

2.4.Pattern

A lattice structure, Figure 1, was designed in SolidWorks and selected as the 3D printed adsorbent geometry. The reason for choosing the lattice structure was its low weight and high porosity. In addition, its interconnected network facilitates the penetration of liquid through the structure. Lattice structures allow for greater contact between the adsorbent and the dye solution, while requiring less material to manufacture. Another advantage of this design is the presence of open channels that allow the solution to pass through different areas of the monolith and improve contact with the existing adsorption sites. Also, the selected geometry can be easily fabricated by DLP printing. In addition to its advantages in adsorption and 3D printing, the network architecture also plays an important role in the acid treatment step. Due to its open and interconnected network, the acid solution can easily penetrate the entire structure, rather than being limited to the outer surface. This allows the printed monolith to be exposed to acid more uniformly. As a result, the lattice geometry not only improves the adsorption performance, but also contributes to a more effective and uniform acid treatment of the printed adsorbent.

2.5.Printing of the prepared inks

The fabrication of the 3D-printed monoliths was carried out using a DLP 3D printer (Photon Ultra, Anycubic, China). A commercial acrylate-based photopolymer resin sensitive to light with a wavelength of $\lambda = 405$ nm was used as the printing material. The layer thickness was set

to 50 μm. To ensure proper adhesion of the first layers to the build platform, a longer exposure time was applied at the beginning of the process. Accordingly, the first four layers were exposed for 60 s, while the subsequent layers were cured for 4 s each. The remaining printing parameters are summarized in monoliths, the samples were post-cured under UV light for 30 min. The final dimensions of the designed monolith were 10 × 10 × 10 mm, as shown in Figure 1.

Table 1.

In the DLP process, each layer is projected as a digital image onto the surface of the photocurable resin, where selective polymerization occurs according to the designed cross-section. After curing each layer, the build platform is lifted slightly to allow fresh resin to flow underneath, enabling the formation of the next layer. This layer-by-layer approach continues until the complete monolithic structure is formed. Since DLP technology cures an entire layer simultaneously, it offers relatively high printing speed while maintaining good resolution compared to other light-based additive manufacturing techniques. After completion of printing, the fabricated structures were detached from the build platform and washed with EtOH to remove any residual uncured resin. The samples were then dried at room temperature. To further complete the curing process and improve the mechanical stability of the printed monoliths, the samples were post-cured under UV light for 30 min. The final dimensions of the designed monolith were 10 × 10 × 10 mm, as shown in Figure 1.

Table 1. Printing details of the monolith.

Printing parameters	**Value**

Layers Thickness	0.050
Normal Exposure Time (s)	4.0
The first layers Exposure Time (s)	60.0
First Layers No.	4

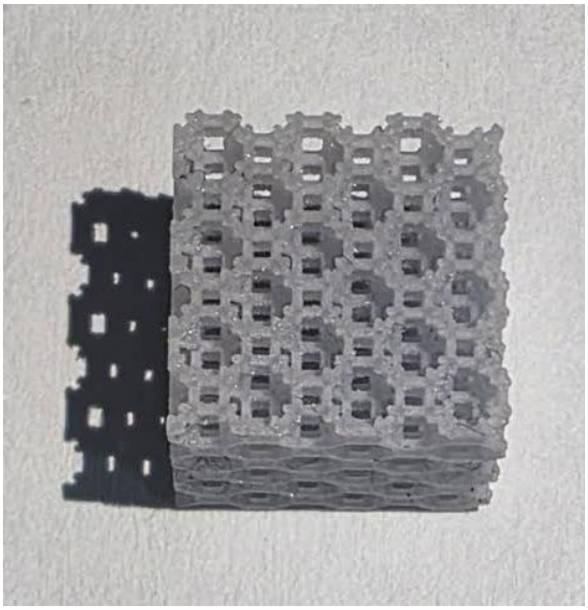


Figure 1: Structure of 3D-Per15 monolith.

2.6.Acid-treatment of 3D-Per15

To acid-treat the synthesized 3D-Per15 monolith, 3D-Per15 was placed in a beaker containing an aqueous solution of sulfuric acid (1.0 M) and heated at 50 °C for 10 h. Upon completion, the acid-treated monolith, 3D-Per15-A (Figure 2), was washed with deionized water and dried at ambient temperature for 12 h.

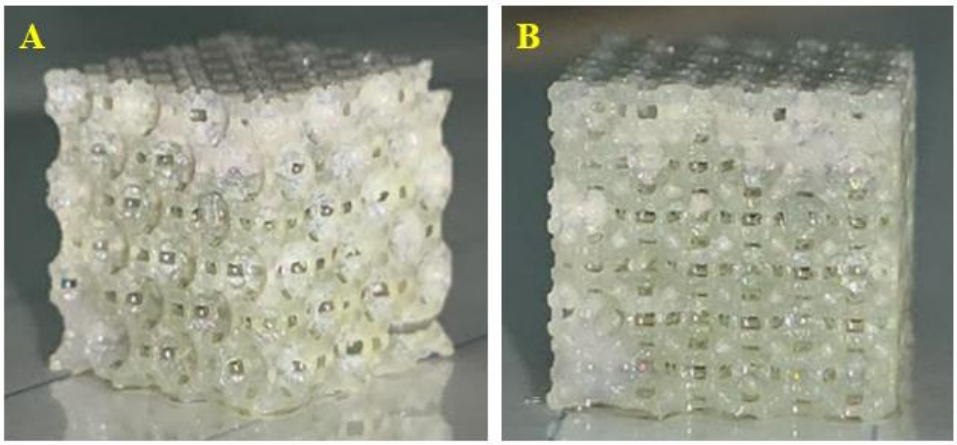


Figure 2: Images of the fabricated 3D-Per15-A: (a) three-quarter view and (b) front view.

2.7.Dye removal

To evaluate the performance of 3D-ptinted adsorbents in each adsorption experiment, 10 mg of each of the dyes (Methylene blue, Rhodamine B, Methyl orange, and Congo red) were added to 1 L of water and placed on a stirrer. Then, 3D-ptinted adsorbent was immersed in this solution. Samples were removed at 10-minute time intervals during stirring to assess the effect of the adsorbent. The absorbance of the fabricated adsorbents was measured to determine the residual dye concentration, and the dye absorption was measured using UV-Vis spectroscopy at proper wavelengths. The effect of pH was observed by studying the adsorption of dye in the pH range from 3 to 11. The pH of the dye solution was adjusted using NaOH and HCl solutions and a pH meter. The adsorption studies were carried out at 85°C. The absorption rate at time (s), qt (mg/g), was calculated using the following formula:

$$q_t = \frac{(C_0 - C_t)V}{m} \qquad \text{(Equation 1)}$$

The initial adsorption of the solution, which corresponds to the initial concentration (C_0), was determined at the beginning of the experiment. Then, by measuring the adsorption of the solution after contact with the adsorbent and applying the Beer-Lambert law, the residual dye concentration (C_t) was calculated based on Equation 2.

$$q_e = \frac{(C_0 - C_e) \times V}{m}$$ (Equation 2)

Where q_e, C_0, C_t, V, m represents the adsorption capacity, initial solution concentration (mg g^{-1}), secondary solution concentration (mg L^{-1}), solution volume (L), adsorbent amount (g), respectively.

The dye removal percentage was calculated using Equations 2 and 3:

$$(\%) \text{ of dye Removal} = \frac{(C_0 - C_e)}{C_0} \times 100$$ (Equation 3)

3. Result and discussion

3.1.Perlite as a potential adsorbent

Perlite is a naturally occurring amorphous aluminosilicate volcanic material that has attracted significant attention in environmental remediation due to its low cost, wide availability, chemical stability, and porous structure [59-61]. The chemical composition of Perlite is predominantly governed by silica (SiO_2) and alumina (Al_2O_3), together with minor quantities of alkali and alkaline-earth oxides, the relative proportions of which may vary depending on the geological source of the mineral [59; 62]. The high content of silica and alumina contributes to the structural integrity of Perlite and provides the fundamental framework responsible for its adsorption properties [59; 60]. The adsorption performance of Perlite is strongly associated with its surface chemistry. The presence of silanol (Si–OH) groups and hydrated aluminum species on the mineral surface creates active adsorption sites capable of interacting with dissolved contaminants through electrostatic attraction, ion exchange, hydrogen bonding, and surface complexation mechanisms [60; 63]. Furthermore, surface hydroxyl groups play a critical role in determining the adsorption affinity of Perlite toward both organic dyes and inorganic pollutants [60; 63; 64].

In addition to surface chemistry, the porous structure and surface morphology of Perlite significantly influence mass transfer and adsorption behavior. Surface defects, irregular pores, broken bonds, and negatively charged sites generated during mineral formation facilitate the diffusion and attachment of pollutant molecules to the adsorbent surface [63]. Consequently, Perlite has been successfully employed for the removal of various contaminants, including dyes, heavy metals, and other hazardous compounds from aqueous environments [60; 62; 64].

Recent studies have demonstrated that surface modification is an effective strategy for enhancing the performance of three-dimensional printed adsorbents. In particular, acid treatment of 3D-printed monolithic structures has been shown to significantly improve adsorption efficiency. For example, an acid-treated 3D-printed GO-g-C_3N_4-geopolymer composite achieved a MB removal efficiency of 90.97%, superior compared with the untreated sample, while exhibiting high stability during repeated use. After five consecutive adsorption cycles, the removal efficiency decreased by only 5%, confirming that acid treatment effectively enhances the durability and long-term performance of 3D-printed monolithic adsorbents. Motivated by these findings, the present study applies acid washing to the optimized 3D-printed Perlite monolith in order to further improve its adsorption performance for wastewater treatment [21].

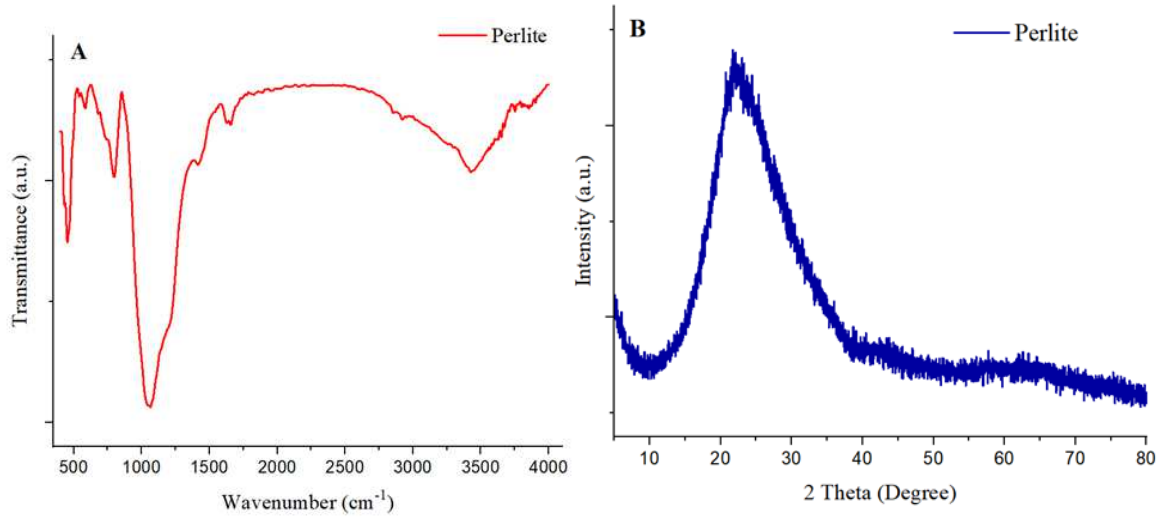
3.2.Characterization of Perlite

As noted, the characteristics of Perlite are highly dependent on the geological source of the mineral. Therefore, the characterization of the Perlite used in this study was carried out.

To characterize Perlite, its FTIR spectrum was investigated. As shown in **Figure *3***A, the absorption band at 460 cm^{-1} is attributed to the rocking motion of the oxygen atom attached to the Si–O–Si plane, while the absorption band at 3407 cm^{-1} is related to the –OH group. The absorption band at 792 cm^{-1} is attributed to the Si–O stretching vibration in Si–O–Al. In

addition, the absorption band at 1059 cm^{-1} can be ascribed to the Si–O–Si or Si–O–Al stretching vibration. XRD analysis was used to investigate the crystalline phases of Perlite (Figure 3B). As shown, since Perlite is composed of amorphous mineral phases, it exhibits a broad band in the range 2θ = 10-34º in the curve.

SEM image of Perlite is shown in Figure 3C. As is clear, this material has a layered and sheet-like structure with broken or uneven edges in the form of flakes [65]. These plates are stacked, and numerous folds are observed on the surface of the particles, which is a well-known characteristic of Perlite. This structure has created a relatively heterogeneous surface. Such a morphology can increase the effective contact area of the material and facilitate the access of contaminant molecules to the active areas.



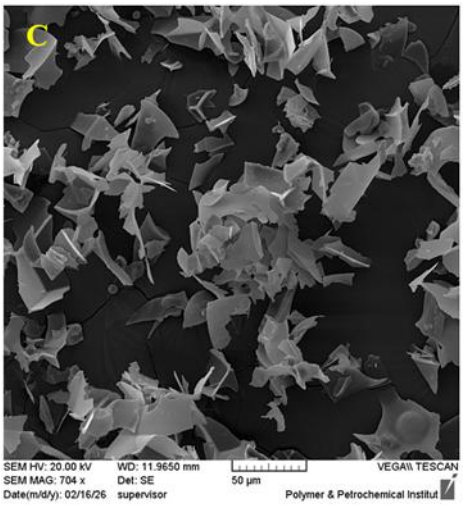


Figure 3: A: FTIR spectrum and B: XRD pattern, and C: SEM image of Perlite

To investigate the surface properties and porosity of Perlite, nitrogen adsorption-desorption measurements were performed at 77 K and the results are summarized in Table 2. As shown in **Error! Reference source not found.** the initial increase in nitrogen adsorption at low relative pressures ($P/P_0 < 0.1$) is attributed to monolayer adsorption on available surface sites, while the gradual increase in adsorption capacity at higher relative pressures is related to multilayer adsorption in the mesopores. The continuous increase in the amount of nitrogen adsorbed at higher relative pressures indicates the contribution of interparticle voids and mesopore channels to the overall pore network. The average pore diameter of Perlite was determined to be 4.03 nm. The presence of mesopores is particularly beneficial for dye adsorption applications, as these pores provide accessible pathways for the diffusion of dye molecules from the bulk solution to the active adsorption sites. Furthermore, the accessible surface area can increase the number of available adsorption sites, thereby increasing the adsorption capacity of the material. The combination of surface accessibility and mesoporous transport channels is expected to facilitate mass transfer and improve the overall efficiency of dye removal from aqueous solutions. BET analysis also revealed a mesoporous volume of 0.55 $cm^3 g^{-1}$.

Table 2. textural analyses of Perlite

Parameter	Value
Mesopore Volume	0.55 cm^3 g^{-1}
BET surface area, S_{BET}	2.43 m^2 g^{-1}
Total pore volume	0.00245 cm^3 g^{-1}
Average pore diameter	4.03 nm

3.3.Characterization of 3D-Perlite

The FTIR spectra of 3D-Per15, 3D-Per10, 3D-Per5, Perlite, and the 3D-resin are compared in Figure 4. Characteristic absorption bands of the 3D-resin are observed at 3434 cm^{-1}, corresponding to the stretching vibration of hydroxyl (–OH) groups, at 2910 and 2854 cm^{-1}, assigned to the asymmetric and symmetric stretching vibrations of aliphatic $–CH_2$ groups, and at 1743 and 1637 cm^{-1}, attributed to the stretching vibrations of carbonyl (C=O) and C–O functional groups, respectively. In all 3D-Per15, 3D-Per10, 3D-Per5 samples, the characteristic bands of resin are observable. Notably, the characteristic bands of Perlite (see 3.2 section) overlapped with those of resin. Hence, FTIR spectroscopy cannot solely confirm the incorporation of Perlite in the 3D-printed samples. In fact, as the main component in 3D-Per15, 3D-Per10, 3D-Per5 samples is ABS-like resin, their FTIR spectra are more similar to that of resin.

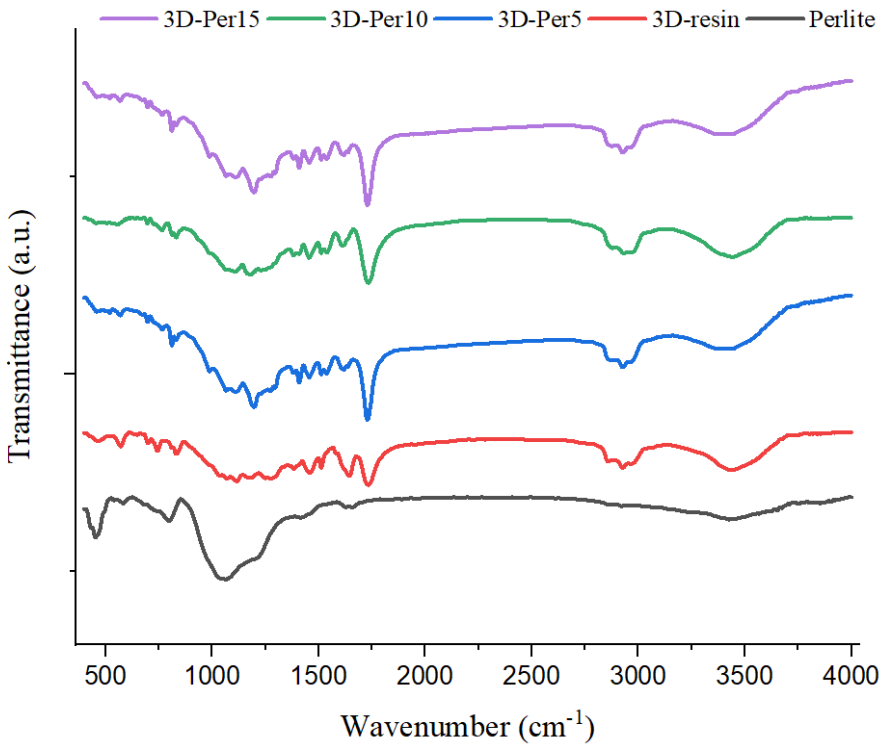


Figure 4: FTIR spectra of 3D-Per15, 3D-Per10, 3D-Per5, Perlite and 3D-resin

The thermal stability of 3D-Per5, 3D-Per10, 3D-Per15 and 3D-resin was investigated via TGA. As shown in Figure Perlite exhibits excellent thermal stability and only shows two minor weight loss stages at approximately 180 °C and 570 °C, which are attributed to the removal of physically adsorbed water and dehydroxylation of its aluminosilicate framework, respectively. In contrast, the 3D-resin shows a slight initial weight loss below 200 °C due to the evaporation of residual moisture and volatile species, followed by a significant weight loss stage associated with the thermal decomposition of the crosslinked polymer network. The TGA curves of 3D-Per5, 3D-Per10, and 3D-Per15 are very similar to those of the 3D-resin, indicating that the thermal degradation behavior of the printed monoliths is mainly controlled by the polymer matrix. All printed monoliths remain almost unchanged below 200 °C, indicating sufficient thermal stability in this temperature range. A slight weight loss is observed at around 250 °C, which can be attributed to the decomposition of unstable functional groups and the onset of

polymer chain degradation. The main decomposition stage occurs between 300 and 500 °C, which is related to the decomposition of the polymer framework.

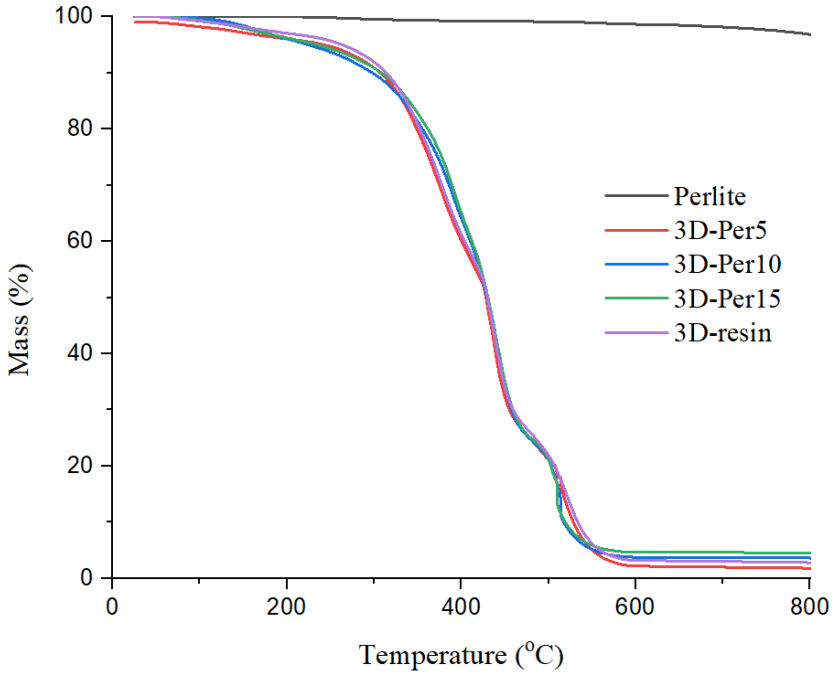


Figure 5: Thermogram of 3D-Per5, 3D-Per10, 3D-Per15, 3D-resin and Perlite

As shown in Figure , the DTG curve of the commercial resin exhibits three degradation peaks at 373, 438, and 513°C, indicating that the resin undergoes a multi-step thermal decomposition process associated with the degradation of different structural components. In contrast, the DTG curves of samples 3D-Per5, 3D-Per10, and 3D-Per15 exhibit two dominant degradation peaks at approximately 440 and 501°C. The similarity of the peak positions among the samples indicates that the incorporation of different amounts of Perlite does not significantly alter the degradation mechanism of the polymer matrix. This can be attributed to the relatively low content of Perlite in the composites, which was not sufficient to have a significant effect on the thermal stability of the polymer matrix.

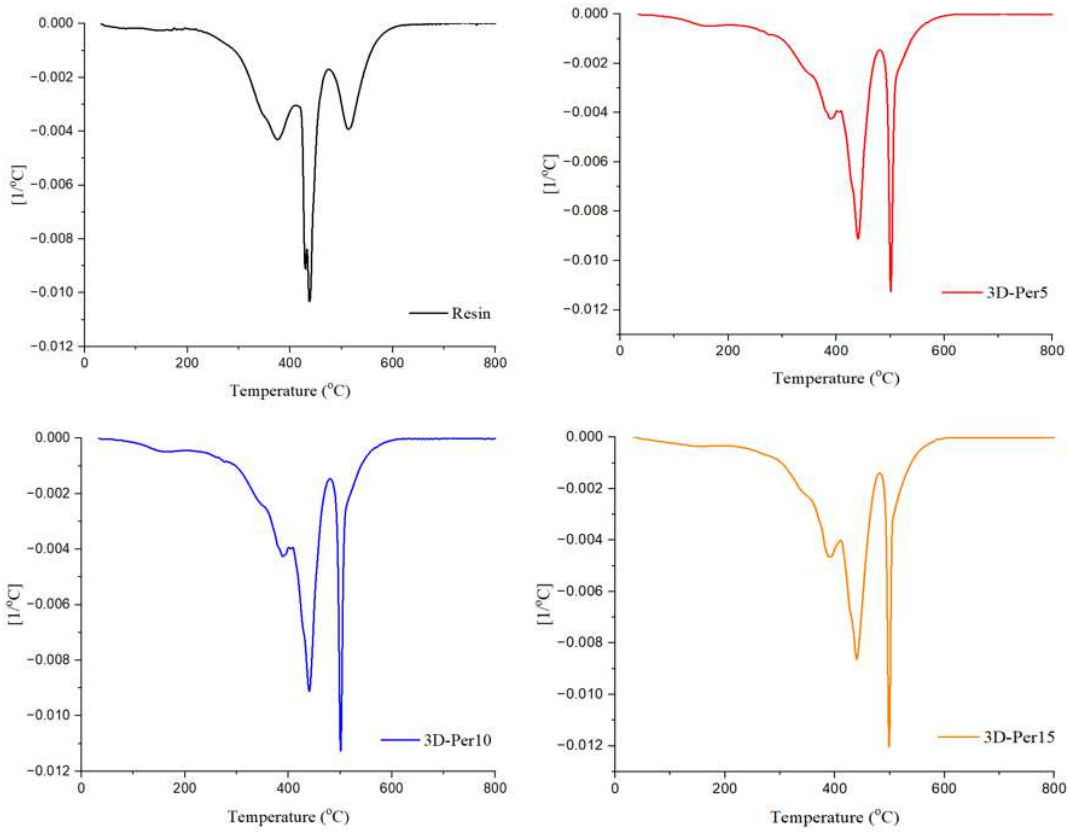


Figure 6: DTG curves of Resin, 3D-Per5, 3D-Per10 and 3D-Per15.

The compressive behavior of the 3D printed samples was evaluated by ISO 604 and the samples were compressed at a constant rate of 2 mm min^{-1} to investigate the effect of adding Perlite on the mechanical performance of the resin matrix. The force-displacement curves are presented in Figure . All samples showed a similar deformation pattern initially, with increasing displacement, the compressive force increased, then reached a maximum value, and subsequently was accompanied by a decrease in force, indicating the occurrence of structural failure under compressive loading. The 3D-resin shows the highest compressive strength (480 N). In the 3D-Per5 monolith, the presence of a small amount of Perlite had a limited effect on the compressive strength of the printed structure. The similarity of the 3D-resin and 3D-Per5 curves indicates that at this loading level, the resin matrix still retains its ability to withstand and transfer applied stresses to a large extent. With increasing Perlite content, a gradual

decrease in compressive strength was observed. So that the maximum compressive strength for samples 3D-Per10 and 3D-Per15 was obtained at about 405 and 304 N, respectively. This decrease can be attributed to the decrease in the continuity of the polymer phase due to the increase in the proportion of mineral particles. In fact, with increasing Perlite content, a part of the continuous resin matrix, which is mainly responsible for load bearing, reduces the ability to effectively transfer stress in the structure due to the decrease in adhesion between layers and stress concentration. Increasing the amount of Perlite may cause local inhomogeneity in the microstructure and provide the basis for the initiation of local deformations and the occurrence of failure at lower stresses. As shown in the curve, the presence of Perlite particles affected the deformation mechanism of the printed structures and changed the way the stress was distributed during compressive loading. Also, the fluctuations observed in the post-failure region for the 3D-Per10 and 3D-Per15 samples could indicate the gradual damage and local collapse of different parts of the structure. In general, increasing the percentage of Perlite leads to a gradual decrease in the compressive performance of the printed monoliths. However, the 3D-Per5 monolith still maintained mechanical properties close to those of the pure resin, while further increasing the amount of Perlite causes a noticeable decrease in load-bearing capacity.

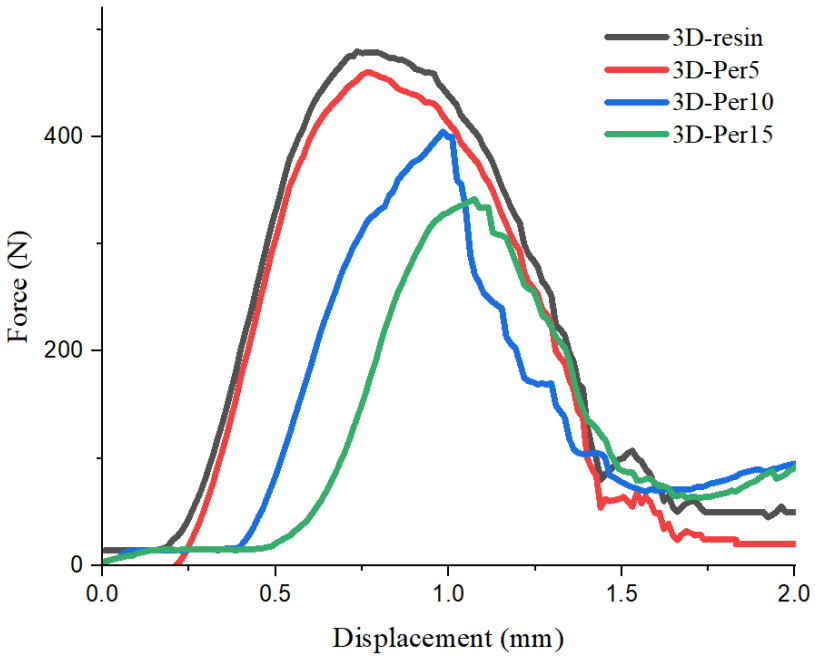


Figure 7. Compressive load-deflection behavior of 3D-Per5, 3D-Per10, 3D-Per15 and 3D-resin

To investigate the crystalline phase and structure of 3D-Per samples, 3D-Per15 was selected as and its XRD pattern was recorded, Figure . The XRD pattern of 3D-Per15 is very similar to XRD of Perlite and shows a broad peak in the range of 2θ=15–35°. This behavior is not only due to the amorphous nature of Perlite, but also is attributed to the amorphous nature of the resin and the formation of a 3D polymer network during the photopolymerization process.

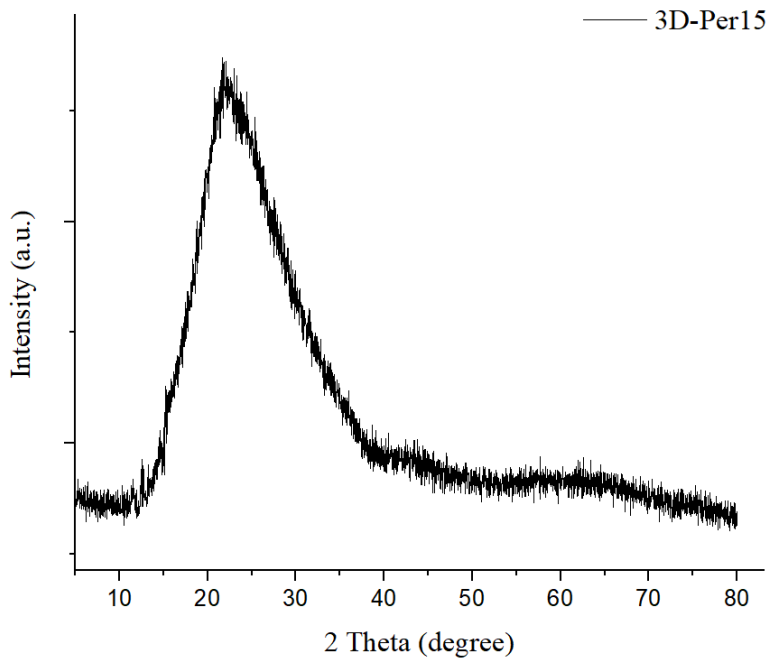


Figure 8: XRD pattern of 3D-Per15

The morphology of the samples was also studied by recording their SEM images and compared with the monolith without Perlite (3D-resin). As shown in Figure A, and E the 3D-resin exhibited a smooth layered surface, while the surface of the other three monoliths was covered with Perlite particles. Figure B, and F show the morphology of the 3D-Per5 monolith at different magnifications. The polymer matrix presents a relatively smooth and continuous surface, while only a limited number of Perlite particles are observed. Most of the particles appear to be embedded in the polymer matrix, indicating that the resin constitutes the dominant surface phase and limits the number of available adsorption sites. In Figure C, and G corresponding to 3D-Per10, the incorporation of a larger amount of Perlite results in a more heterogeneous surface morphology. Compared to 3D-Per5, a larger number of mineral particles can be detected on the composite surface, leading to an increased surface roughness. Figure D, and H show the morphology of the 3D-Per15 monolith. At this level of Perlite loading, the surface becomes significantly rougher and a larger number of Perlite particles are deposited on the composite surface. This morphology increases the possibility of direct interaction between

MB molecules and active Perlite adsorption sites. Furthermore, the relatively uniform particle distribution indicates that increasing the Perlite content did not result in significant particle aggregation or structural defects.

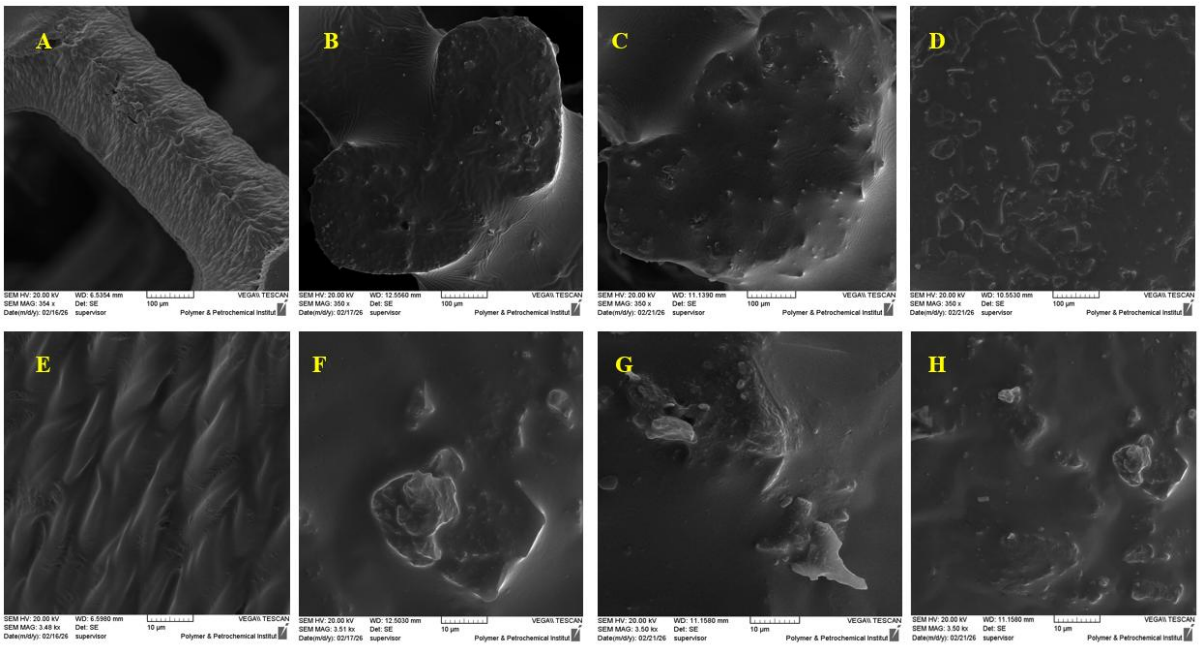


Figure 9: SEM images of 3D-resin (A and E), 3D-Per5 (B and F,), 3D-Per10 (C and G), 3D-Per15 (D and H)

To further characterize 3D-Per15, EDS and elemental mapping analyses were performed. As shown in Figure 4A, the elements Ca, Si, Al, O, Fe, K, and Na can be attributed to the Perlite structure, while the C and O atoms can be attributed to the printing resin. Figure 4B confirmed the homogeneous distribution of Perlite in the 3D printed monolith, confirming that ultrasonication was effective for its dispersion in the resin.

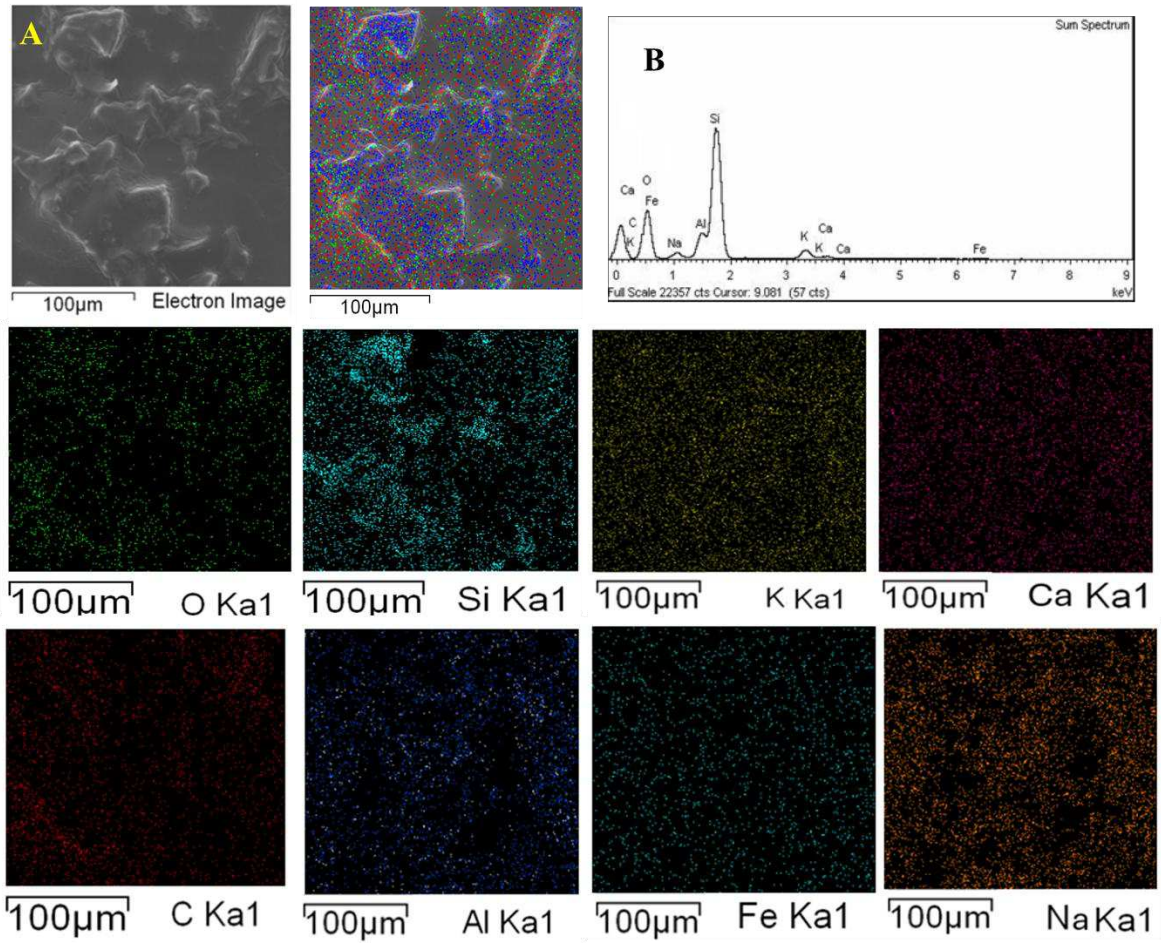


Figure 4: A: EDS results of 3D-Per15 and B: Elemental mapping of 3D-Per15

3.4.Adsorption potential of 3D-Per15

3.4.1. Role of 3D-printing in adsorption

The primary objective of this study was to combine the intrinsic adsorption capability of Perlite with the advantages offered by three-dimensional printing technology to develop an efficient monolithic adsorbent for MB removal. Although Perlite has attracted considerable attention as an adsorbent owing to its porous structure, low cost, and availability, its powdered form suffers from several practical drawbacks, including difficult separation from aqueous media, loss of adsorbent during operation, and limited reusability. Therefore, transforming powdered Perlite into a monolithic structure through 3D printing could provide an effective strategy to overcome these limitations while preserving its adsorption performance. To evaluate the actual

contribution of the printing process to the adsorption behavior, the MB removal performance of 3D-Per15 was compared with that of the corresponding 3D-printed polymer matrix without Perlite under identical experimental conditions, Figure 5. The obtained results revealed that the blank printed polymer exhibited a certain degree of adsorption toward MB. This behavior may be attributed to the physical entrapment of dye molecules within the polymeric network as well as possible interactions between MB molecules and the functional groups present in the printed matrix. However, the adsorption efficiency of 3D-Per15 was significantly higher than that of the Perlite-free printed structure, clearly demonstrating the essential role of Perlite as the active adsorptive component. This observation confirmed that the 3D-printing process did not adversely affect the accessibility of the active sites of Perlite. In other words, embedding Perlite particles within the polymeric framework did not hinder the diffusion of MB molecules toward the adsorption sites, and the dye molecules were still able to efficiently interact with the active surfaces of the adsorbent.

Furthermore, the role of 3D printing extended beyond simply shaping the adsorbent into a recoverable monolithic form. The well-defined architecture generated during the printing process may facilitate mass transfer by providing accessible diffusion pathways, thereby enhancing the contact between dye molecules and the active sites. In addition, the crosslinked polymeric network effectively immobilized the Perlite particles within the monolith and prevented their detachment or leaching during the adsorption process. Such structural stability is particularly advantageous for improving the reusability and long-term applicability of the adsorbent. These findings suggest that 3D printing played a dual role in the performance of the 3D-Per15 system. First, it enabled the conversion of powdered Perlite into an easily recoverable monolithic adsorbent with improved handling properties. Second, it contributed to maintaining, and potentially enhancing, the overall adsorption performance by creating a stable and

interconnected structure that allowed efficient diffusion of MB molecules toward the embedded active particles.

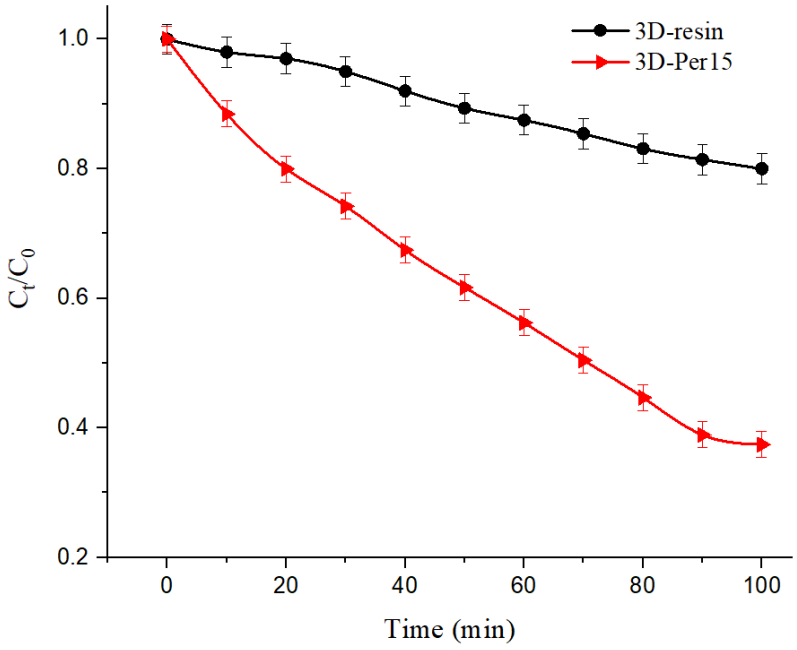


Figure 5: Comparison of the efficiency of 3D-resin and 3D-Per15 for MB removal. Reaction conditions: MB solution initial concentration: 10 mg L^{-1}, temperature: 85 ºC, time up to 100 min.

1.1.1. Effect of Perlite loading on the adsorption capacity

As mentioned above, 3 samples, i.e. 3D-Per5, 3D-Per15, 3D-Per15, with different loadings of Perlite were prepared and their adsorption capacities for MB were compared under similar conditions (MB solution initial concentration: 10 mg L-1, temperature: 85 ºC, time up to 100 min). According to the results, the adsorption efficacy followed the order of 3D-Per15>3D-Per15>3D-Per5, indicating the important role of Perlite loading in adsorption. These results can be justified by the comparison of the characteristics of the aforesaid samples. More accurately, the SEM analysis of the three samples underlined the gradual increase in surface roughness and higher deposition of Perlite particles on 3D-Per15, which is consistent with the adsorption results. Indeed, the improved adsorption performance of

3D-Per15 can be attributed to the greater accessibility of Perlite particles to the dye molecules. High dispersion of Perlite particles with no significant aggregation can also enhance the MB adsorption in 3D-Per15. It is worth noting that further increase of Perlite in printing ink resulted in sedimentation of Perlite particles in the course of 3D-printing and consequently fabrication of a heterogeneous monolith. Hence, the best 3D-printed adsorbent was selected to be 3D-Per15.

1.1.2. Effect of acid treatment: comparison of the adsorption capacity of 3D-Per15 and 3D-Per15-A

3D-Per15 was selected for further surface modification due to its higher adsorption capacity. To further improve its adsorption efficiency, an acid wash treatment was applied with the aim of creating surface microcracks, increasing the accessibility of active adsorption sites, and facilitating mass transfer in the monolithic structure. To investigate the effect of acid washing on the morphology of monoliths, SEM testing was performed. The surface morphology of the 3D-Per15-A monolith is presented in **Error! Reference source not found.**. SEM images of the 3D-Per15-A monolith (Figure12A–C) show significant morphological changes after acid treatment. The polymer surface becomes significantly rougher and contains a greater number of surface asperities, microcracks, and pores, exposing a larger portion of the mineral surface to the surrounding environment. These microstructural modifications increase the accessibility of adsorption sites and facilitate the diffusion of dye molecules into the porous structure of the composite.

Furthermore, the presence of microcracks can create additional diffusion pathways and allow the dye solution to more easily penetrate the inner regions of the monolithic adsorbent. As a result, a larger fraction of the active adsorption sites is available for interaction with MB molecules. This increased accessibility, together with the increased surface roughness and

porosity caused by acid treatment, explains the superior adsorption performance of the 3D-Per15-A monolith compared to 3D-Per15 without acid treatment.

Overall, SEM observations show that acid treatment effectively modified the surface morphology of the printed composite by creating a rougher and more porous structure with additional microcracks and exposed pearlite particles. These structural changes are consistent with the higher adsorption capacity observed for the acid-treated sample and confirm that surface activation via acid treatment is an effective strategy to improve the adsorption performance of 3D printed pearlite-based monoliths.

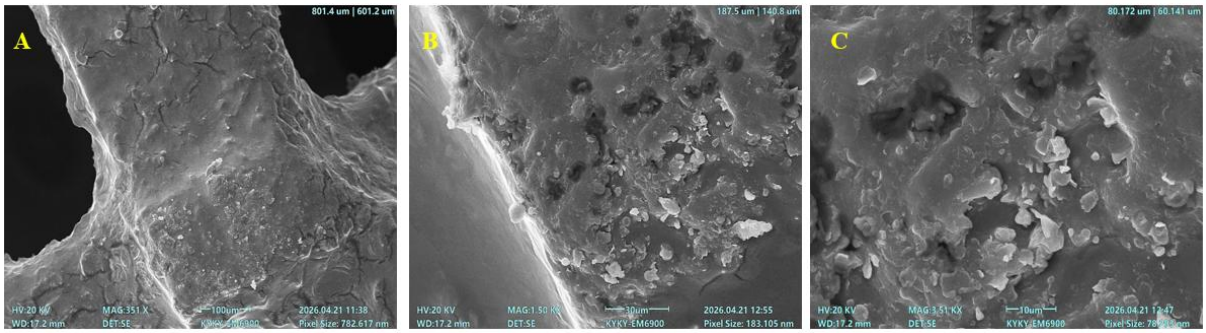


Figure 6: SEM images of 3D-Per15-A (A-C)

To investigate the effect of acid treatment on the strength of the printed monolith, a compressive strength test was performed. The results of samples 3D-Per15-A and 3D-Per15 are presented in Figure 7. As can be seen, sample 3D-Per15 showed a higher compressive strength than sample 3D-Per15-A. This decrease can be attributed to the surface modification caused by the acid treatment, which partially changed the surface of the sample and increased its roughness and porosity. These structural changes weaken the interfacial adhesion between the Perlite particles and the polymer matrix, leading to a lower resistance to compressive loading. Furthermore, as SEM observations showed, the 3D-Per15-A monolith exhibited a rougher surface with the formation of additional microcracks and pores. These microstructural defects could act as stress concentration sites during compression and facilitate crack initiation

and propagation under applied load. As a result, the mechanical integrity of the printed monolith was slightly reduced after acid treatment, resulting in a lower compressive strength compared to the 3D-Per15. Although the compressive strength was slightly reduced after acid treatment, the printed monolith maintained sufficient mechanical stability for reuse and exhibited improved adsorption performance.

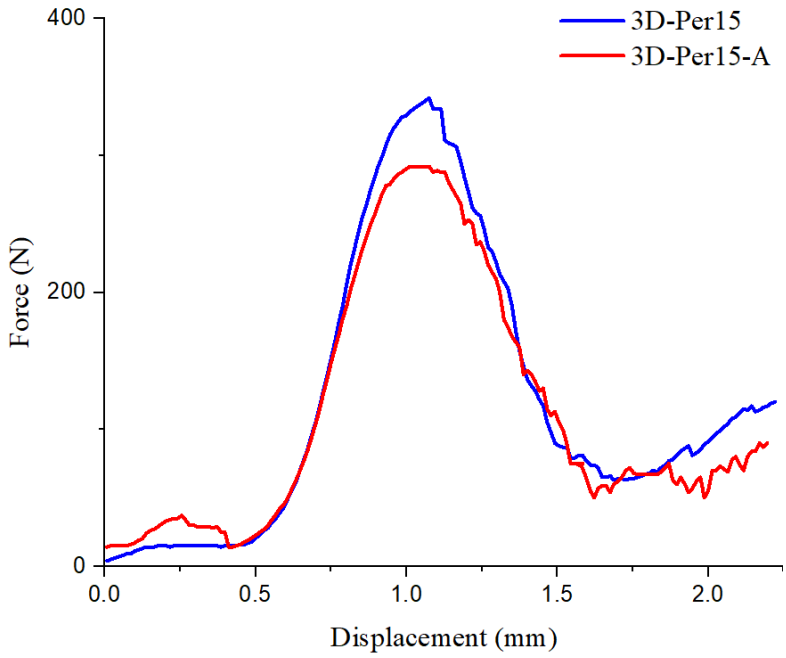


Figure 7: Compressive load-deflection behavior of 3D-Per15 and 3D-Per15-A

The XRD patterns of 3D-Per15 and 3D-Per15-A are presented in Figure 8. Both monoliths show a broad peak at 2θ=15–35°, indicating that the printed monoliths are amorphous as previously mentioned. After acid treatment, no new peaks or significant peak shifts were observed, indicating that the composite structure remained unchanged during the acid activation process. This indicates that the acid treatment did not cause the formation of new crystalline phases or change the bulk structure of Perlite. Only a slight decrease in diffraction intensity was observed, which may be attributed to the removal of surface impurities and slight modification of the outer surface of Perlite particles. The XRD results indicate that the acid

treatment modified the surface characteristics of the composite and preserved its structural framework.

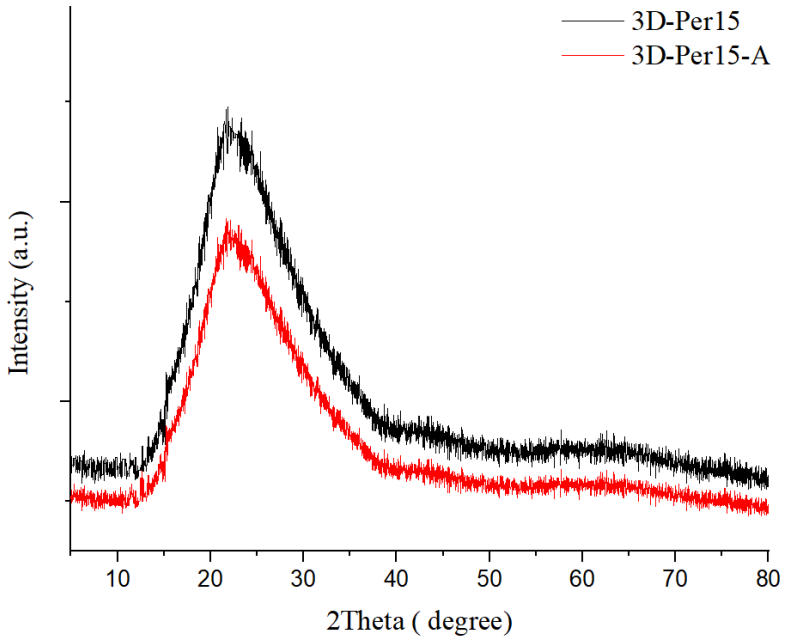


Figure 8: XRD pattern of 3D-Per15 and 3D-Per15-A

The FTIR spectra of 3D-Per15 and 3D-Per15-A monoliths were evaluated to investigate the effect of sulfuric acid pickling on the chemical structure of the composite (Figure 9). In 3D-Per15, the absorption band at 3425 cm^{-1} is attributed to the stretching vibration of (O-H) related to water and silanol groups (Si–OH), while in 3D-Per15-A, this band is shifted to 3375 cm^{-1}. This shift to lower wavenumbers indicates the increase in hydrogen interactions and an increase in surface hydroxyl groups as a result of the removal of impurities from the Perlite surface by sulfuric acid. The bands at 2927 cm^{-1} in the 3D-Per15 and 2935 cm^{-1} in the 3D-Per15-A are related to the stretching vibration of the (C–H) bonds of the resin. Also, the band at 1729 cm^{-1} observed in both monoliths is assigned to the stretching vibration of the (C=O). In the 3D-Per15, the bands at 1619, 1455, and 1409 cm^{-1} are attributed to the C=C vibration, bending vibrations of the methylene, and methyl groups, respectively. In the 3D-Per15-A, the same bands are observed, and only their slight shift indicates a change in the chemical environment

of the surface groups after acid washing without changing the main structure of the polymer matrix.

These changes indicate that sulfuric acid has been used to remove mineral impurities and partially dissolve non-silicate phases, as well as increase the number of active groups, while maintaining the chemical structure of the resin. This surface modification could have improved the adsorption performance of the acid-washed monolith.

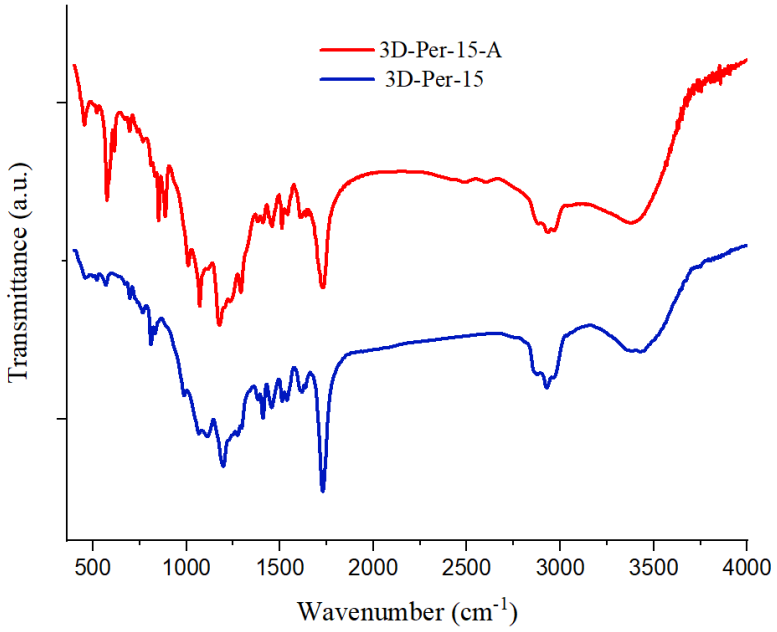


Figure 9: FTIR spectra of 3D-Per15 and 3D-Per15-A

The BET test results showed that acid washing with sulfuric acid had a significant effect on the properties of the 3D-Per15 composite. As can be seen in Table 3, after acid washing, the BET specific surface area increased from 3.2117 to 10.522 $m^2 g^{-1}$, indicating an increase in the active surface area during the adsorption process.

In addition, the mesopore volume increased from 0.7379 to 2.4174 $cm^3 g^{-1}$, indicating a significant expansion of the mesoporous network and the opening of pores that were blocked before acid washing. Also, the increase in the total pore volume from 0.006 to 0.008 $cm^3 g^{-1}$ indicates an increase in the available space for the penetration and transport

of dyes molecules in the adsorbent structure. These changes facilitate mass transfer, increase the permeability of methylene blue molecules, and increase the number of accessible active sites, all of which are effective factors in improving the adsorption capacity. Although the average pore diameter has decreased from 7.79 to 3.19 nm, the decrease in the average pore diameter does not mean the destruction of the porous structure, but rather indicates the formation of a larger number of fine and uniform mesopores as a result of the acid washing process.

The creation of such a structure significantly increases the specific surface area without losing the ability of dye molecules to penetrate into the pores. The simultaneous increase in specific surface area, mesopore volume, and total pore volume clearly indicates that acid washing has played a very effective role in modifying the surface structure of 3D-Per15. This structural modification has increased the number of active sites, improved mass transfer, and provided more contact surface between the adsorbent and MB molecules. Therefore, the adsorption performance of the 3D-Per15-A monolith has been significantly improved compared to the original sample. Therefore, the BET results well confirm that acid washing was one of the most important factors in increasing the adsorption efficiency in this composite. These results are in complete agreement with the adsorption test data and indicate that the increase in the adsorption performance of the acid- washed sample is mainly due to the increase in the specific surface area, the development of the mesoporous structure, and the increase in the number of active sites created by the acid washing process.

Table 3: BET test results of 3D-Per15 and 3D-Per15-A

	Value	
Parameter	**3D-Per15**	**3D-Per15-A**
Mesopore Volume	0.73 $cm^3\ g^{-1}$	2.41 $cm^3\ g^{-1}$

BET surface area, S_{BET}	3.21 $m^2 g^{-1}$	10.52 $m^2 g^{-1}$
Total pore volume	0.0062577 $cm^3 g^{-1}$	0.0084 $cm^3 g^{-1}$
Average pore diameter	7.79 nm	3.198 nm

1.1.3. Effect of temperature

Temperature is one of the key parameters influencing the dye adsorption process. In general, variations in temperature can significantly affect adsorption kinetics, mass transfer behavior, and the interaction between dye molecules and the adsorbent surface. The effect of temperature on dye adsorption onto 3D-Per15-A was investigated over a temperature range of 25 to 95 °C with 10 °C intervals, and an optimum temperature of 85 °C was identified, Figure 10. The experimental results demonstrated that increasing the temperature from 25 to 85 °C led to a considerable enhancement in both dye removal efficiency and adsorption capacity. This improvement can be attributed to the increase in the kinetic energy of dye molecules, which promotes more frequent and effective collisions between dye species and the active sites on the Perlite surface. In addition, higher temperatures reduce the viscosity of the solution, thereby facilitating mass transfer and accelerating the diffusion of dye molecules into the internal porous structure of the adsorbent. Moreover, an increase in temperature may improve the accessibility of active adsorption sites. At elevated temperatures, enhanced molecular mobility allows dye molecules to more easily penetrate into the inner pores of the adsorbent, which contributes to the overall improvement in adsorption performance. In some cases, thermal effects may also lead to improved exposure of surface area, further supporting the adsorption process. Although in most physical adsorption systems an increase in temperature typically results in a reduction in adsorption capacity due to the weakening of intermolecular interactions, the present study exhibited an opposite trend up to 85 °C. This suggests that in the

current system, the enhancement in diffusion and mass transfer processes dominates over the possible decrease in adsorption affinity at higher temperatures.

However, further increasing the temperature to 95 °C did not lead to a significant improvement in adsorption performance, indicating that the system approaches equilibrium or partial saturation of active sites under these conditions. Finally, considering both energy consumption and adsorption efficiency, 85 °C was selected as the optimum temperature, as it provides a suitable balance between process performance and energy requirements.

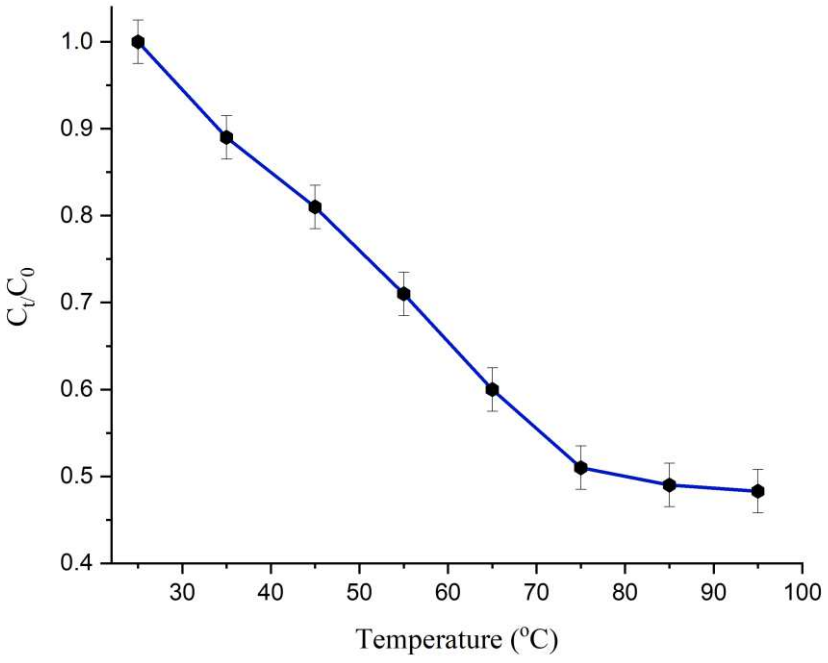


Figure 10: Investigation of the influence of temperature on the adsorption of MB using 3D-Per15-A, MB solution initial concentration: 10 mg L^{-1}, time up to 100 min.

1.1.4. Effect of contact time

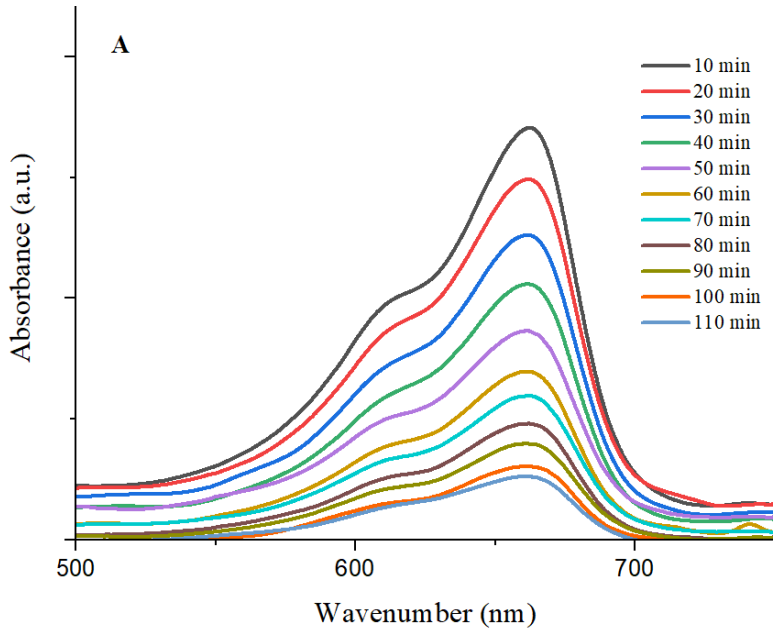
Time is another crucial parameter governing the adsorption performance of dyes onto porous materials. The effect of contact time on the removal of MB was investigated using 3D-Per15-A as the adsorbent. To evaluate the adsorption behavior, a dye solution with 10 mg L^{-1}

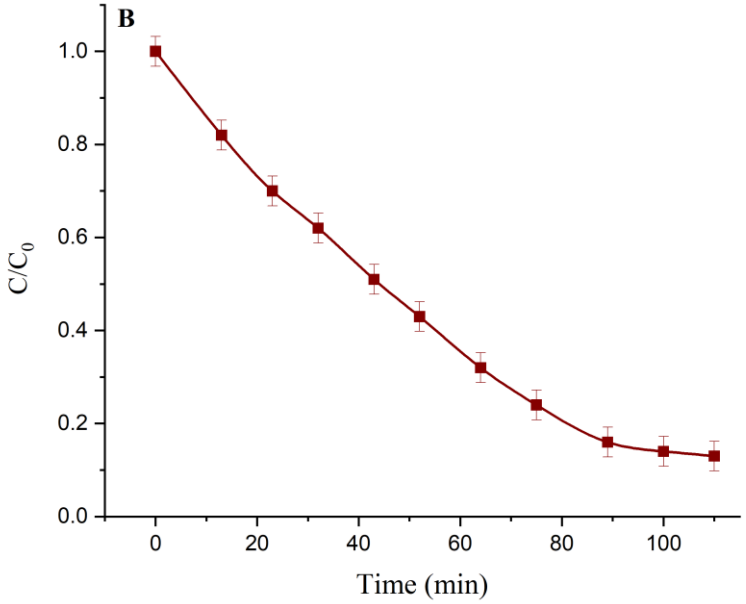
concentration was prepared, and the removal efficiency was monitored over a period of up to 110 min. UV–Vis spectroscopy measurements were performed at regular 10 min intervals, Figure 11A and B specifically at the characteristic absorption λ_{max}=665 nm for MB.

The results indicated that the adsorption process was strongly time-dependent, particularly during the initial stages. According to the obtained data, both dye removal efficiency and adsorption capacity increased progressively with increasing contact time up to 100 min. This behavior can be attributed to the availability of a large number of vacant active sites on the Perlite surface at the beginning of the process, which facilitates rapid uptake of dye molecules. In addition, the high concentration gradient between the bulk solution and the adsorbent surface at early times provides a strong driving force for mass transfer, resulting in a fast initial adsorption rate. As the contact time increases, the number of available active sites gradually decreases due to their occupation by MB molecules. Consequently, the adsorption rate declines, which can be explained by increased repulsive interactions between adsorbed and free dye molecules as well as diffusion limitations within the internal porous structure of the adsorbent. In the later stages of the process, the system gradually approaches equilibrium, and no significant improvement in dye removal is observed beyond 100 min. This indicates that most of the accessible adsorption sites have already been occupied and that the adsorption–desorption processes tend toward dynamic equilibrium. Therefore, extending the contact time further does not lead to a meaningful enhancement in adsorption performance.

Based on these findings, the optimum contact time for MB removal using 3D-Per15-A was determined to be 100 min. Overall, these results highlight the importance of contact time in governing adsorption kinetics and confirm that the process is initially dominated by rapid surface adsorption, followed by a gradual transition to a diffusion-limited and equilibrium-controlled stage. More accurately, the adsorption capacity increased to 17.8 mg g^{-1} with prolonged contact time. According to the results, the maximum removal efficiency of 89% was

recorded in 100 minutes. It is worth noting that the color of 3D-Per15-A monolith altered from gray to a bluish color, Figure 11C, visually approves the successful adsorption of MB dye throughout the monolith.





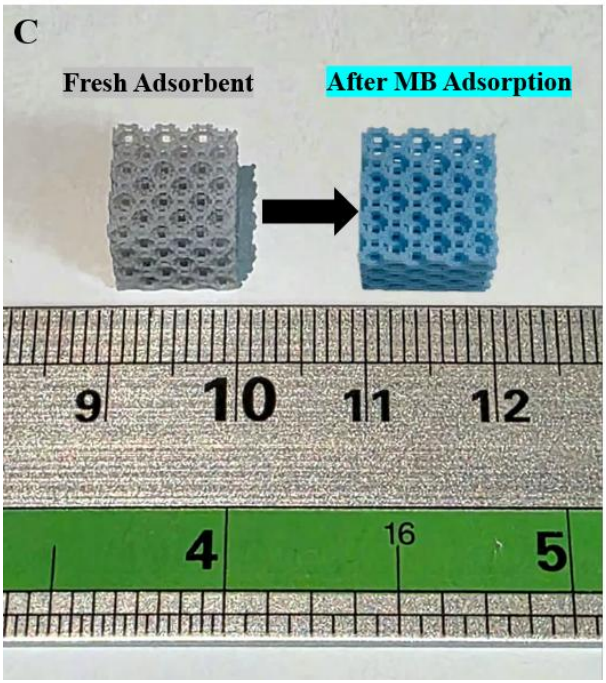


Figure 11: Investigation of the influence of contact time on the adsorption of MB using 3D-Per15-A. A: UV-Vis absorption spectra of MB at λ_{max}=665 nm and B: variation of MB concentrations with time during adsorption by 3D-Per15-A, C: color change of fresh 3D-Per15-A from gray to blue upon MB adsorption. Reaction conditions: MB solution initial concentration: 10 mg L^{-1}, temperature: 85ºC.

1.1.5. Effect of pH

The influence of solution pH on the adsorption performance of 3D-Per15-A was also investigated. To this end, the adsorption of MB was evaluated at different pH values, including acidic (pH = 3 and 5), neutral (pH = 7), and basic conditions (pH = 9, 10, and 11), Figure 12. The adsorption experiments were carried out for 100 min, and the residual concentration of MB was determined using UV–Vis spectroscopy. The obtained results demonstrated that the adsorption efficiency of 3D-Per15-A was strongly dependent on the pH of the solution. According to the results, 3D-Per15-A exhibited its lowest adsorption performance under acidic conditions, whereas the adsorption efficiency improved progressively with increasing pH and

reached its maximum value at pH = 10. More accurately with increasing pH, the q_t reached 15.34 mg g^{-1}.

Since MB is a cationic dye, this behavior can be explained by considering the surface charge characteristics of the adsorbent. Under acidic conditions, the high concentration of H^+ ions lead to protonation of the active sites on the adsorbent surface. As a result, H^+ ions compete with MB molecules for the available adsorption sites, thereby reducing the interaction between the dye molecules and the adsorbent and consequently decreasing the adsorption efficiency.

In contrast, increasing the pH of the solution reduces the competition from hydrogen ions and promotes the development of negatively charged sites on the surface of 3D-Per15-A. The enhanced electrostatic attraction between the negatively charged adsorbent surface and the positively charged MB molecules facilitates the adsorption process and leads to higher dye uptake. Furthermore, the reduced protonation of the adsorbent surface under alkaline conditions increases the availability of active sites for interaction with MB molecules. The experimental findings revealed that the adsorption capacity increased gradually as the pH increased from acidic to alkaline values and reached its optimum value at pH = 10. However, further increasing the pH from 10 to 11 did not result in any significant enhancement in adsorption performance, indicating that the adsorption process had reached its maximum efficiency under the studied conditions. Therefore, pH = 10 was selected as the optimum pH for subsequent adsorption experiments.

Overall, these results confirm that solution pH plays a critical role in regulating the adsorption behavior of MB onto 3D-Per15-A by affecting both the surface properties of the adsorbent and the electrostatic interactions governing the adsorption process. The superior performance observed at pH 10 suggests that alkaline conditions provide the most favorable environment for the adsorption of cationic MB molecules onto the 3D-Per15-A adsorbent.

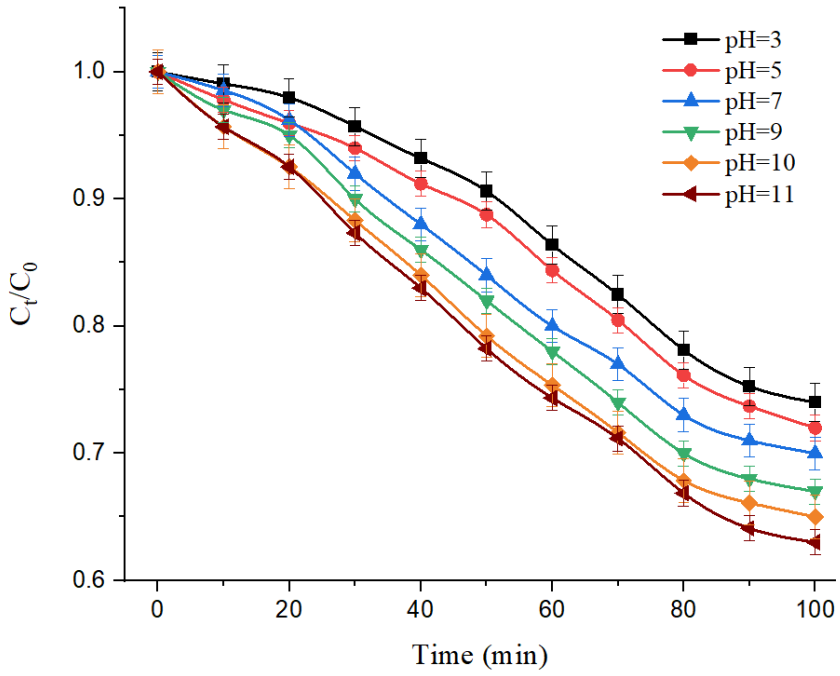


Figure 12: Investigation of the influence of different pH values on the adsorption of MB using 3D-Per15-A, MB solution initial concentration: 10 mg L^{-1}, time up to 100 min.

1.2.Generality study

To further assess the adsorption versatility of the fabricated 3D-Per15-A, its performance toward the removal of dyes with different ionic characteristics was investigated under the optimized adsorption conditions (temperature = 85 °C, contact time = 100 min, initial dye concentration = 10 mg L^{-1}). Besides MB, which exhibited the highest removal efficiency (89%), three additional model dyes, RhB, MO, and CR (Figure 19), were evaluated to better understand the adsorption selectivity of the prepared adsorbent. As illustrated in Figure , 3D-Per15-A exhibited superior adsorption performance toward cationic dyes. RhB was removed with an efficiency of approximately 72%, which, although lower than that of MB, still demonstrates the high affinity of the adsorbent toward positively charged dye molecules. The slightly lower uptake of RhB can be attributed to its bulkier molecular structure and larger molecular dimensions, which increase steric hindrance and reduce the accessibility of

adsorption sites located within the porous structure of the adsorbent. Consequently, the diffusion of RhB molecules into the internal pores is less favorable than that of the relatively smaller MB molecules. In contrast, the adsorption efficiencies for the anionic dyes were considerably lower. MO and CR exhibited removal efficiencies of approximately 63% and 45%, respectively. This behavior can primarily be explained by electrostatic interactions. Under the strongly alkaline conditions employed in this study (pH = 10), the surface hydroxyl groups of the Perlite-based adsorbent become deprotonated, resulting in the formation of negatively charged surface sites. These negatively charged sites promote electrostatic attraction toward cationic dyes while simultaneously generating electrostatic repulsion against anionic dye molecules, thereby suppressing their adsorption. Although both MO and CR are anionic dyes, a noticeable difference in their adsorption behavior was observed. CR exhibited substantially lower removal efficiency than MO, which is mainly attributed to its larger molecular size, elongated structure, and the presence of two sulfonate groups. These structural characteristics not only intensify electrostatic repulsion but also hinder the diffusion of CR molecules into the porous network of 3D-Per15-A because of steric constraints.

In comparison, the relatively smaller molecular structure of MO allows easier access to the available adsorption sites, leading to a higher adsorption efficiency. Overall, the adsorption behavior followed the order MB (89%) > RhB (72%) > MO (63%) > CR (45%), indicating that both the surface charge of the adsorbent and the physicochemical characteristics of the dye molecules, including molecular size, geometry, and ionic nature, play decisive roles in controlling the adsorption process. These findings demonstrate that the 3D-Per15-A monolithic adsorbent possesses excellent selectivity toward cationic pollutants while still maintaining moderate removal capability for anionic dyes, highlighting its potential as an efficient and reusable adsorbent for the treatment of dye-contaminated wastewater containing pollutants with different molecular structures.

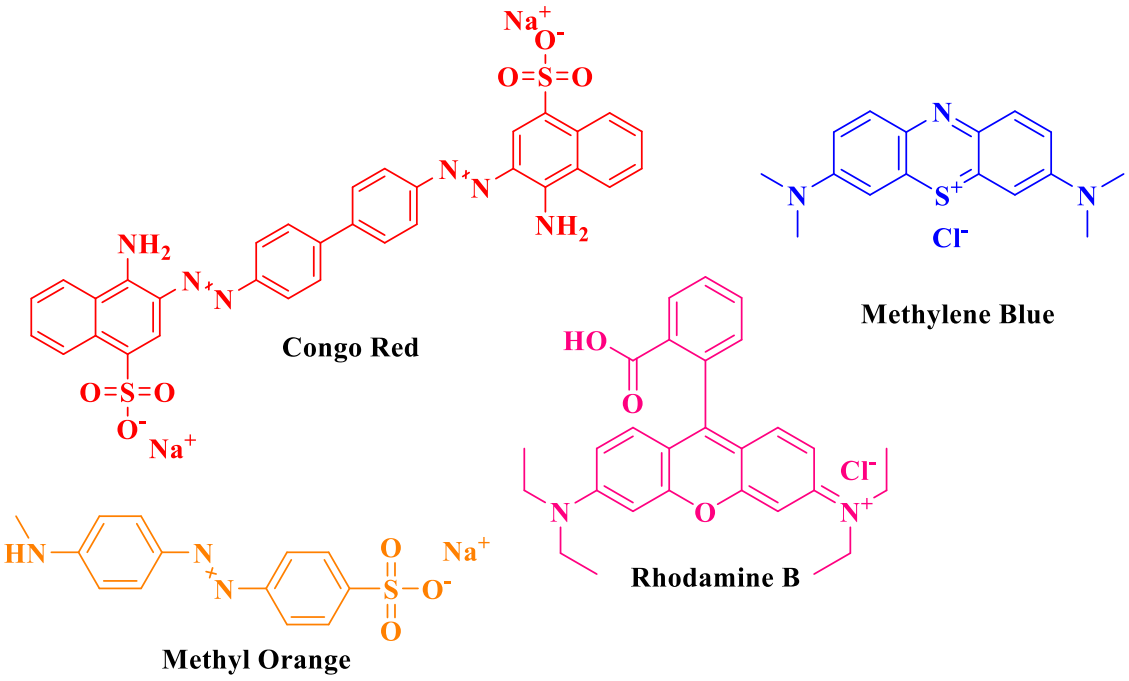


Figure 19: Structure of dyes: Chemical structure of Congo red, Methylene blue, Methyl orange, and Rhodamine B

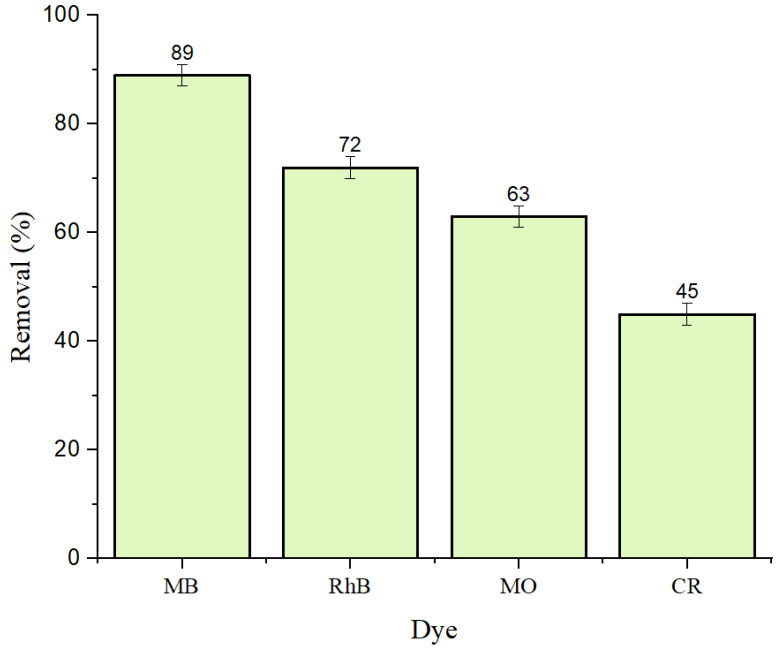


Figure 13: Comparison of the efficiency of 3D-Per15-A for removal of various cationic and anionic organic dyes.

1.3.Kinetic studies

The adsorption kinetics of MB onto the 3D-Per15-A adsorbent were systematically investigated to gain a deeper understanding of the adsorption mechanism and the rate-controlling steps involved in the process. Kinetic analysis is an essential tool for evaluating the interaction between adsorbate molecules and the active sites available on the adsorbent surface.

To assess the adsorption behavior, a series of experiments was carried out at different temperatures while monitoring the variation in dye concentration as a function of contact time. The concentration changes were determined using UV–Vis spectroscopy by measuring the absorbance of MB at its characteristic maximum absorption wavelength. As adsorption proceeded, a gradual decrease in absorbance was observed, indicating the progressive removal of dye molecules from the aqueous solution. The adsorption rate was evaluated. According to the Beer–Lambert law, absorbance is directly proportional to dye concentration; therefore, the ratio of absorbance at a given time (A_t) to the initial absorbance (A_0) can be considered equivalent to the concentration ratio (C_t/C_0). Based on this relationship, the apparent adsorption rate constant (k_{app}) was calculated using Equations (4) and (5). These kinetic parameters provide valuable information regarding the adsorption efficiency, temperature dependence of the process, and the possible adsorption mechanism governing MB uptake by the 3D-Per15-A structure.

$$\frac{dC_t}{dt} = -k_{app}C_t \qquad \text{(Equation 4)}$$

$$\ln {}^{C_t}/_{C_0} = {}^{\ln A_t}/_{A_0} = -k_{app}t \qquad \text{(Equation 5)}$$

The apparent adsorption rate constants (k_{app}) were obtained from the slope of the linear plots of ln (A_t/A_0) versus contact time (t). The calculated k_{app} values at different temperatures (308.15, 318.15, 328.15, 338.15, 348.15, 358.15, and 363.15 K) are summarized in **Error!**

Reference source not found.. As the temperature increased, the apparent rate constant also increased, indicating a faster adsorption process under elevated thermal conditions. This behavior can be attributed to the enhancement of molecular mobility and diffusion of methylene blue molecules in solution at higher temperatures. The increase in thermal energy promotes more frequent and effective interactions between the dye molecules and the available adsorption sites on the surface of the 3D-Per15-A adsorbent. Furthermore, higher temperatures may facilitate mass transfer and reduce diffusion resistance, leading to accelerated adsorption kinetics. These results suggest that the adsorption process is thermally favored and that temperature plays a significant role in improving the adsorption performance of the fabricated 3D-Per15-A.

Table 4. Kinetic and thermodynamic parameters for the adsorption of MB by 3D-Per15-A

Dye	Temperature (K)	1/T (1/K)	k (min^{-1})	Ln (k)	Ln (k/T)	E_a (kJ/mol)	$\Delta G^{\#}$ (kJ/mol)	$\Delta H^{\#}$ (kJ/mol)	$\Delta S^{\#}$ (J/mol.K)
MB	308.15	0.00324	0.25	-1.39	-6.52	27.14±0.6	78.56±0.2	24.36±0.3	-175.91±0.1
	318.15	0.00314	0.43	-0.84	-6.00		80.32±0.2		
	328.15	0.00309	0.67	-0.4	-5.58		82.08±0.2		
	338.15	0.00295	1.05	0.04	-5.22		83.84±0.2		
	348.15	0.00287	1.13	0.12	-4.97		85.60±0.2		
	358.15	0.00279	1.22	0.19	-4.82		87.36±0.2		
	363.15	0.00275	1.27	0.25	-4.75		88.24±0.2		

The activation energy (E_a) for the adsorption of MB onto the 3D-Per15-A was determined using the Arrhenius equation (Equation 6). To this end, a plot of ln(k) versus 1/T was constructed, and the activation energy was calculated from the slope of the resulting straight line (Figure 14) as 27.14±0.6 kJ/mol. The Arrhenius plot exhibited good linearity with an R^2 value of 0.94,

indicating a strong dependence of the adsorption rate on temperature within the investigated range.

This result suggests that increasing the temperature enhances the adsorption rate, which can be attributed to the greater mobility of dye molecules and their improved access to the available adsorption sites. The satisfactory agreement between the experimental data and the Arrhenius model further confirms that temperature plays an important role in controlling the adsorption kinetics of MB on the 3D-Per15-A.

$$\ln k = \ln A - \left(\frac{E_a}{RT}\right) \qquad \text{(Equation6)}$$

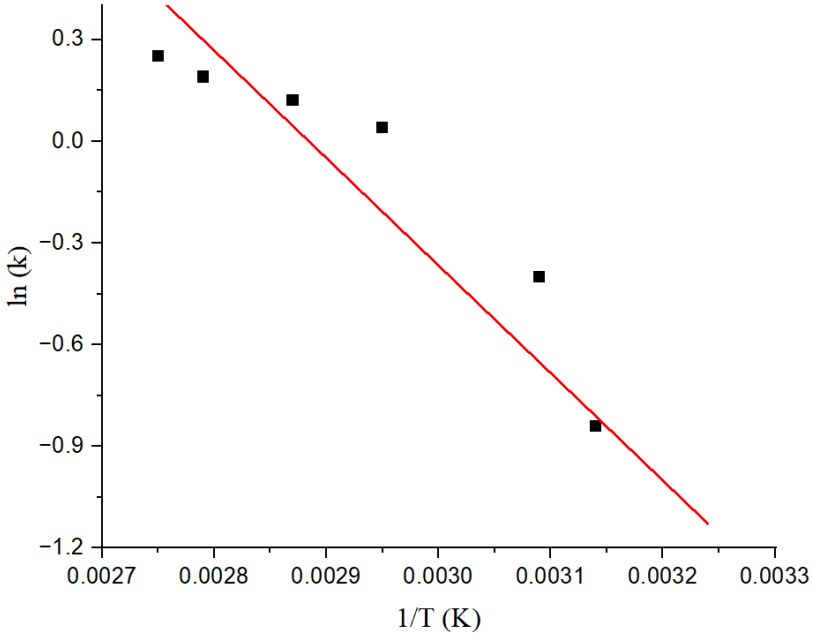


Figure 14: Plot of ln k vs 1/T (Arrhenius equation)

After that, the thermodynamic parameters of the reaction, including the activation entropy ($\Delta S^{\#}$) and activation enthalpy ($\Delta H^{\#}$), were calculated using the Eyring equation (Equation 7).

$$\ln\left(\frac{k}{T}\right) = \ln\left(\frac{k_B}{h}\right) + \frac{\Delta S^{\#}}{R} - \frac{\Delta H^{\#}}{R\left(\frac{1}{T}\right)} \qquad \text{(Equation 7)}$$

In this analysis, k_B represents the Boltzmann constant ($1.381 \times 10^{-23} JK^{-1}$, while h denotes the Planck constant ($6.26 \times 10^{-34} JK^{-1}mol^{-1}$).

The kinetic parameters were evaluated using the Eyring equation by constructing a plot of ln(k/T) versus 1/T (Figure 15). The obtained linear relationship exhibited a high degree of fit, with a determination coefficient of R^2=0.96 for the adsorption of MB, indicating that the experimental data are well described by the model. From the slope and intercept of this plot, the activation parameters were determined. The activation enthalpy ($\Delta H^{\#}$) was calculated to be 24.36 kJ/mol, while $\Delta S^{\#}$ was estimated to be -175.91$\pm$0.1 J/mol.K

The positive value of $\Delta H^{\#}$ for the 3D-Per15-A confirms that the adsorption process is endothermic in nature. This behavior is consistent with a predominantly physical adsorption mechanism governing the interaction between the dye molecules and the adsorbent surface, and it also aligns with the observed decrease in adsorption capacity at elevated temperatures. Overall, these findings suggest that the adsorption of MB onto 3D-Per15-A proceeds with a favorable kinetic profile, characterized by a relatively low energy barrier, which supports an efficient adsorption process under the studied conditions.

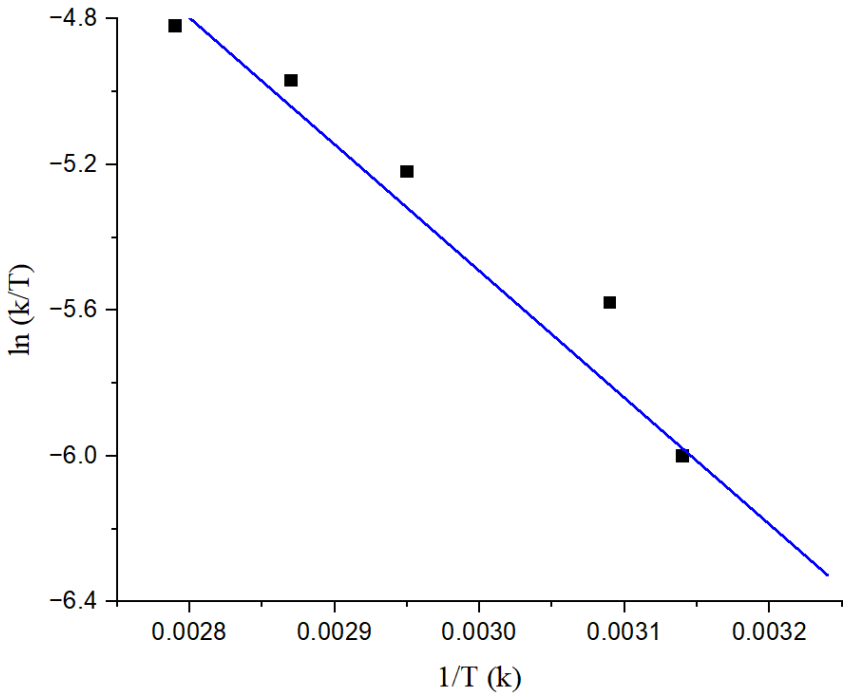


Figure 15: Plot of ln (k/T) k vs T/1 (Eyring equation)

A comprehensive understanding of adsorption kinetics is crucial for elucidating the mechanism of pollutant removal and identifying the factors governing the adsorption rate. Kinetic studies provide important information regarding the interaction between adsorbate molecules and the active sites of the adsorbent, as well as the mass-transfer phenomena involved during the adsorption process. Since the adsorption performance is highly dependent on the structural and surface characteristics of the adsorbent, kinetic modeling can offer valuable insight into the dominant adsorption pathways. In this study, the experimental results were analyzed using pseudo-first-order, pseudo-second-order, and intraparticle diffusion kinetic models.

The pseudo-first-order model (Figure 16), first introduced by Lagergren, assumes that the adsorption rate is proportional to the number of vacant adsorption sites available on the adsorbent surface. This model is generally associated with adsorption processes in which external mass transfer plays a significant role. According to the model, the adsorption capacity at equilibrium is represented by q_e (mg g^{-1}), whereas q_t (mg g^{-1}) corresponds to the adsorption

capacity at any adsorption time (t). The parameter k_1 (min^{-1}) is the pseudo-first-order rate constant, reflecting the rate at which adsorption occurs under the assumptions of the model.

$$\log\ (q_e - q_t) = \log q_e\ - \frac{k_1 t}{2.303} \qquad \text{(Equation 8)}$$

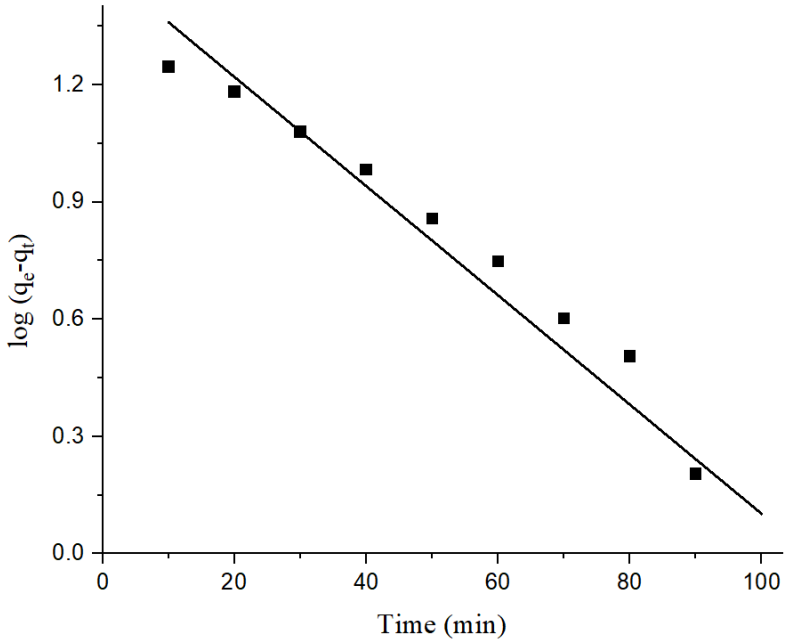


Figure 16: Pseudo-first-order kinetic of dye adsorption

The pseudo-second-order model (Figure 17) was also employed to evaluate the adsorption kinetics. This model assumes that the adsorption rate depends on the availability of adsorption sites and is related to the square of the number of unoccupied sites on the adsorbent surface. Following integration of the rate equation, the kinetic parameters can be determined from the linearized form of the model, Equation 9. In this equation, K_2 (g $mg^{-1}.min^{-1}$) denotes the pseudo-second-order rate constant. Due to its ability to accurately describe many adsorption systems, this model is widely used to investigate adsorption mechanisms and adsorption-rate behavior.

$$\frac{t}{q_t} = \frac{1}{k_2 {q_e}^2} + \left(\frac{1}{q_e}\right) t \qquad \text{(Equation 9)}$$

To further clarify the diffusion characteristics of the system, the intraparticle diffusion model was applied (Figure 18). This model evaluates whether the migration of adsorbate molecules within the internal pores of the adsorbent contributes significantly to the adsorption process.

$$q_t = \mathrm{k_p t^{0.5}} + \mathrm{I} \qquad \text{(Equation 10)}$$

In the model equation 10, K_p (mg g^{-1} $min^{-1/2}$) represents the intraparticle diffusion rate constant, while I (mg g^{-1}) correspond to the intercept associated with the boundary-layer effect. The magnitude of this intercept reflects the thickness of the boundary layer, with higher values indicating a stronger contribution of external mass-transfer resistance.

Based on the kinetic analysis, the pseudo-second-order model provided the best correlation with the experimental data (R^2 = 0.996), suggesting that surface interaction processes play a dominant role in the adsorption mechanism.

Although the pseudo-first-order model showed a relatively acceptable agreement, its lower correlation coefficient (R^2 = 0.947) indicates that it does not fully capture the adsorption behavior of the system, Table 5.

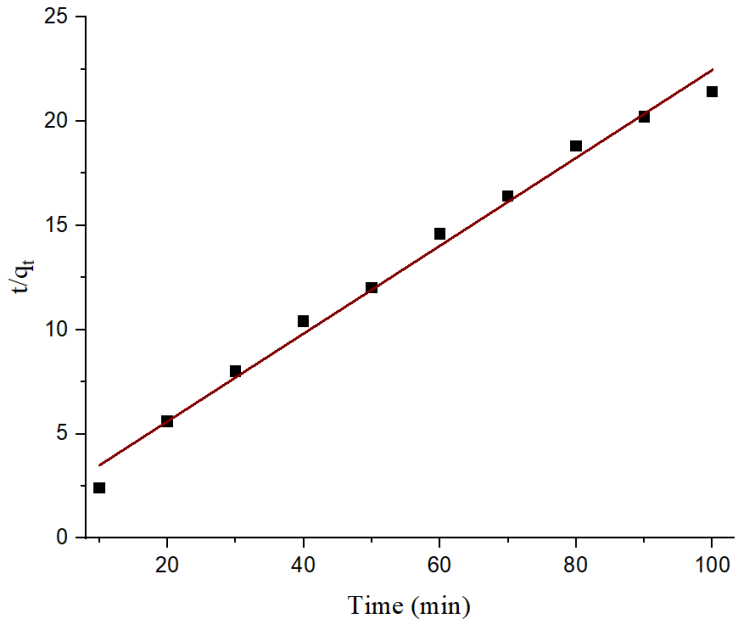


Figure 17: Pseudo second-order kinetic of dye adsorption

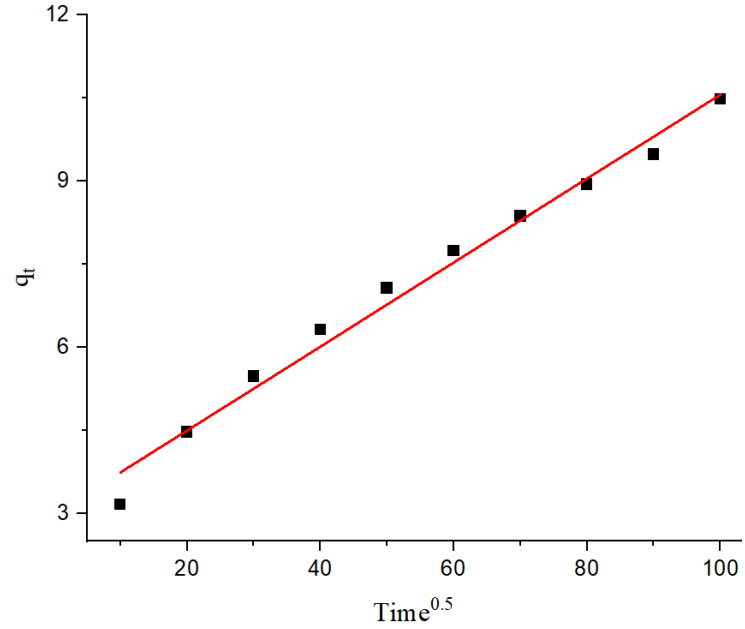


Figure 18: Intraparticle diffusion kinetic of dye adsorption

Table 5. Kinetic parameters of MB adsorption by 3D-Per15-A

Dye	Adsorbent	Pseudo-first order			Pseudo-second order			Intraparticle Diffusion		
		q	k_1	R^2	q	K_2	R^2	k_p	I	R^2
MB	3D-Per15-A	16.4	0.0322	0.947	17.6	0.0241	0.996	2.53	8.1	0.984

1.3.1. Adsorption Isotherms

Adsorption isotherms are widely used to describe the interaction between adsorbate molecules and the adsorbent surface, particularly in the removal of organic contaminants. These models provide important insights into whether the adsorption process occurs through monolayer or multilayer coverage, as well as the energetic heterogeneity of the surface. In the present work, the equilibrium adsorption behavior of methylene blue onto the 3D-Per15-A adsorbent was investigated using the Langmuir and Freundlich isotherm models, which offer complementary descriptions of surface–adsorbate interactions.

The Langmuir isotherm model is based on the assumption of monolayer adsorption on a structurally uniform surface with a finite number of identical active sites. According to this model, each adsorption site accommodates only one adsorbate molecule, and no interaction occurs between adsorbed species. Although idealized, this model is widely applied for interpreting equilibrium adsorption data in liquid-phase systems. In this framework (Eq. 11), C_e (mg L^{-1}) represents the equilibrium concentration of the adsorbate in solution, q_0 (mg g^{-1}) denotes the maximum monolayer adsorption capacity, and K_L (mg L^{-1}) is the Langmuir affinity constant describing the strength of interaction between adsorbate and adsorbent. The parameter

q_e (mg g^{-1}) corresponds to the amount of adsorbate retained at equilibrium concentration. The linear form of the Langmuir equation is expressed as:

$$q_e = q_0 K_L C_e/(1 + K_L C_e) \quad \text{(Equation 11)}$$

In contrast, the Freundlich isotherm is suitable for heterogeneous and reversible adsorption systems. It accounts for variations in surface adsorption energy with increasing surface coverage and considers interactions among adsorbed molecules. The empirical Freundlich equation is given by:

$$\log q_e = \log K_F + \left(\frac{1}{n}\right) \log C_e \quad \text{(Equation 12)}$$

In contrast, the Freundlich isotherm is an empirical model that describes adsorption on heterogeneous surfaces where the adsorption energy is not uniformly distributed. This model assumes the possibility of multilayer adsorption and considers the variation in binding site energies across the adsorbent surface. The Freundlich equation is characterized by two parameters: K_F (L g^{-1}), which reflects the adsorption capacity of the system, and 1/n, which indicates the adsorption intensity and surface heterogeneity. Values of $(0 < 1/n < 1)$suggest favorable adsorption conditions, whereas $(1/n > 1)$ indicates less favorable uptake behavior. When n=1, adsorption becomes linear and independent of concentration.

The equilibrium adsorption behavior of 3D-Per15-A was evaluated using both models, as summarized in Table . The experimental results revealed a rapid uptake of MB at the initial stage, attributed to the abundance of available active sites on the adsorbent surface. As these sites gradually became occupied, the adsorption rate decreased until equilibrium was reached.

Regarding the equilibrium isotherm analysis, the Langmuir model yielded a maximum adsorption capacity of approximately 18.2 mg g^{-1} with a high correlation coefficient (R^2= 0.981), indicating that monolayer adsorption on a finite number of homogeneous sites is a reasonable approximation for the system. Meanwhile, the Freundlich model also provided a

good fit (R^2 = 0.975), reflecting the presence of surface heterogeneity and non-uniform distribution of adsorption energies on the 3D-Per15-A surface.

Overall, the combined kinetic and isotherm analyses suggest that the adsorption of MB onto 3D-Per15-A is governed by a hybrid mechanism involving strong surface interactions and heterogeneous adsorption sites. The consistency between the pseudo-second-order kinetics and the Langmuir isotherm further supports the predominance of surface-controlled adsorption with significant contribution from chemisorption-like interactions, while the Freundlich behavior confirms the non-uniform nature of the adsorbent surface.

Table 6. Isotherm parameters of MB adsorption by 3D-Per15-A

Isotherm	Parameter	Adsorbent
		3D-Per15
Langmuir	Q_0	18.2
	K_L	0.084
	R^2	0.981
Freundlich	K_F	6.73
	1/n	0.41
	R^2	0.975

1.4.Recyclability

One of the key advantages of employing 3D printing technology in the fabrication of the 3D-Per15-A adsorbent lies in its ability to transform a powder-based functional material into a mechanically robust monolithic structure, thereby significantly simplifying the separation and recovery process after adsorption. In this context, the 3D-Per15-A exhibited excellent structural

integrity under continuous agitation conditions and could be readily retrieved from the aqueous solution without the need for complex separation procedures.

To evaluate the regeneration capability and practical applicability of the material, the adsorbent was subjected to six consecutive adsorption–desorption cycles under fixed operational conditions, including an initial MB concentration of 10 mg L^{-1}, a contact time of 100 min, and a temperature of 85 °C (Figure 19). After each adsorption step, the monolith was regenerated and subsequently reused in the next cycle without additional chemical modification. The recycling experiments demonstrated that 3D-Per15-A maintained a considerable fraction of its initial adsorption performance throughout multiple operational cycles, indicating good structural stability and sustained functional activity. The gradual decline in adsorption efficiency observed with increasing cycle number can be attributed to the partial occupation of active sites and the difficulty in fully restoring all adsorption centers after repeated dye uptake. In particular, strong interactions between methylene blue molecules and the active functional groups of the adsorbent may lead to irreversible binding on a fraction of the surface sites, thereby contributing to the observed reduction in performance.

The excellent recyclability of the 3D-Per15-A monolith is strongly related to the uniform distribution of the active phase within the polymeric resin matrix during the 3D printing process. This homogeneous incorporation minimizes material loss during operation and preserves the structural integrity of the adsorbent throughout repeated use. From a practical standpoint, such stability is highly desirable for continuous or semi-continuous water treatment applications, where repeated regeneration and operational durability are critical performance criteria. Overall, the results confirm that 3D-Per15-A is a promising reusable adsorbent platform with stable structural properties and satisfactory reusability over multiple adsorption cycles, highlighting its potential for sustainable and scalable wastewater treatment applications.

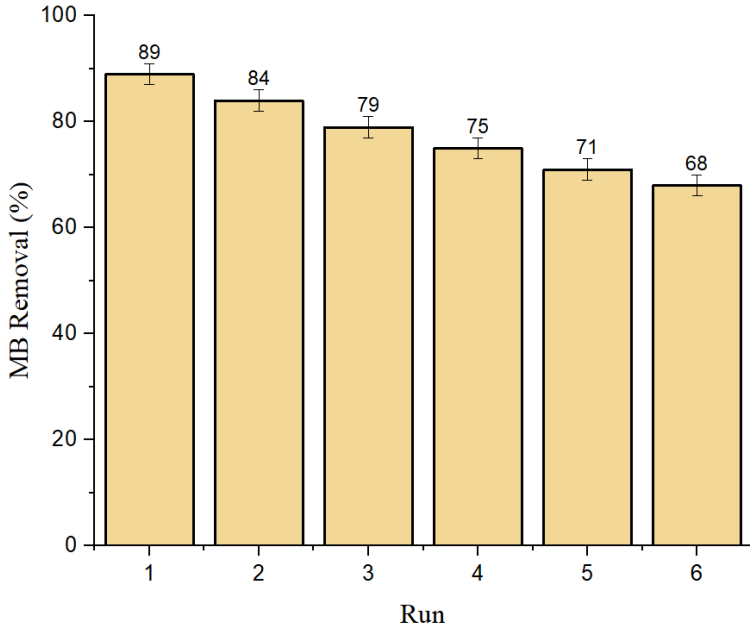


Figure 19: Investigation of the recyclability of 3D-Per15-A for MB adsorption

1.5.Characterization of recycled 3D-Per15-A

The chemical stability of 3D-Per15-A after recycling was further evaluated by FTIR spectroscopy. As shown in Figure 20, the FTIR spectra of fresh and recycled 3D-Per15-A monoliths was almost similar, and the characteristic absorption bands of the fresh sample were preserved after the recycling process. Furthermore, no significant shift in the position of the bands or significant changes in their intensity were observed, indicating that the chemical structure of the composite remained intact during repeated recycling cycles. These findings demonstrate the excellent chemical stability of 3D-Per15-A and confirm its suitability for repeated use in MB adsorption applications.

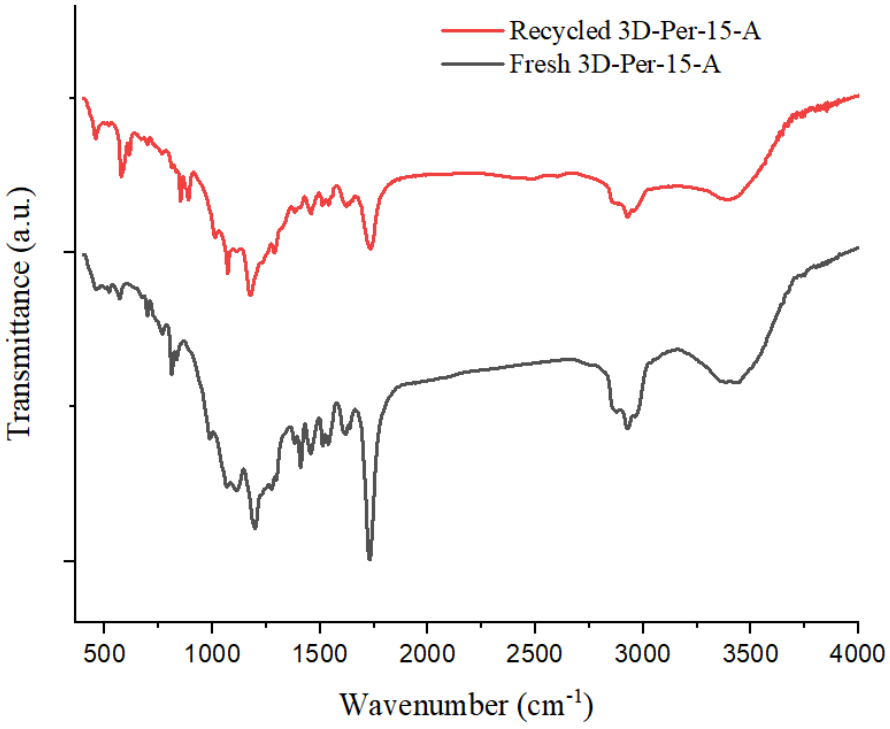


Figure 20: FTIR spectra of fresh and recycled 3D-Per15-A

To further evaluate the effect of the recycling process on the mechanical stability of the adsorbent, the compressive strength of the fresh 3D-Per15-A monolith and the recycled 3D-Per15-A after six cycles were measured and compared (Figure). As shown, the recycled D-Per15-A showed lower compressive strength than the fresh 3D-Per15-A. This decrease can be attributed to the gradual microstructural degradation of the composite during the recycling process. Repeated exposure to aqueous environments during recycling, combined with initial acid treatment, may increase the formation of surface microcracks and microstructural defects and gradually weaken the interfacial adhesion between the Perlite particles and the resin matrix. As a result, the stress transfer at the filler-matrix interface is reduced, leading to a decrease in the compressive strength of the composite. However, the recycled monolith maintained its structural integrity without significant macroscopic fracture or collapse, indicating that despite the moderate reduction in mechanical strength, the 3D-Per15-A adsorbent retains sufficient mechanical strength for repeated recycling applications. It is worth noting that the recycled 3D-

Per15-A preserved its structural integrity in the course of recycling and did not collapse, Figure 20.

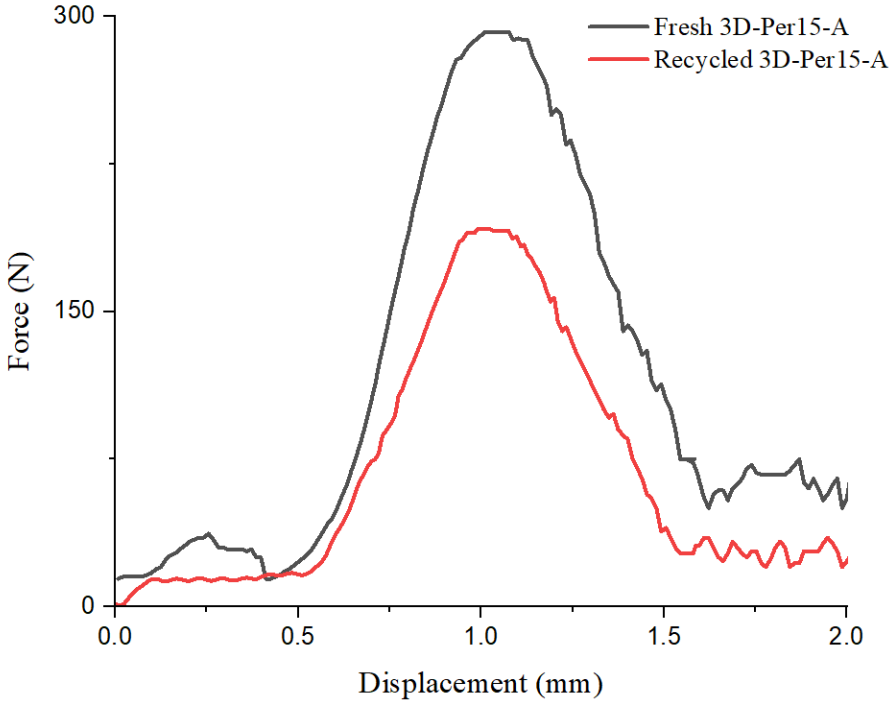


Figure 28: Comparative analysis of fresh and recycled 3D-Per15-A

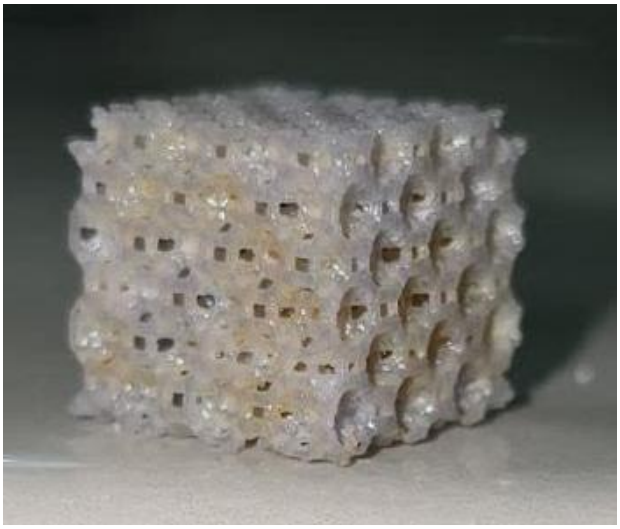


Figure 29: Visual image of recycled 3D-Per15-A

Conclusion

In this study, three 3-dimensional printed Perlite monolithic adsorbents, 3D-Per5, 3D-Per10 and 3D-Per15, with different loadings of Perlites were fabricated through DLP technology and systematically evaluated for the adsorption of MB dyes from aqueous solutions. Comparison of the characteristics of the samples underlined the importance of the loading of Perlite in adsorption capacity and the best performance was obtained for 3D-Per15. To further increase the adsorption capacity of 3D-Per15, it was acid treated to furnish 3D-Per15-A. Characterization of 3D-Per15-A indicated its improved BET specific surface area and porous structure compared to 3D-Per15.

The experimental findings demonstrated that 3D-Per15-A exhibited excellent adsorption performance toward MB (removal efficiency of 89% and a maximum adsorption capacity of 17.8 mg g^{-1}) under the optimized conditions (pH=10, Temp. = 85 °C and time= 100 min), while maintaining satisfactory efficiency after six consecutive regeneration cycles.

Kinetic, equilibrium, and thermodynamic analyses confirmed that the adsorption process was predominantly described by the pseudo-second-order kinetic model and the Langmuir isotherm, indicating favorable adsorption on energetically uniform active sites. The relatively low activation energy (27.14 kJ mol^{-1}), together with the positive thermodynamic parameters (ΔH = 24.36 kJ mol^{-1} and ΔS = −179.91 J mol^{-1} K^{-1}), further verified that the adsorption process proceeded efficiently under the investigated conditions. The 3D-Per15-A monolithic adsorbent also exhibited remarkable selectivity toward dyes with different ionic characteristics. Higher removal efficiencies were achieved for cationic dyes than for anionic dyes. This behavior is attributed to the combined influence of the negatively charged adsorbent surface under alkaline conditions, the increased availability of active adsorption sites generated by acid treatment, and the molecular size and steric characteristics of the dye molecules. These results demonstrate

that both surface modification and three-dimensional structural design contribute significantly to the adsorption performance.

Unlike conventional powdered Perlite adsorbents, the developed 3D-Per15-A combines the advantages of acid activation with additive manufacturing technology. DLP printing eliminates the practical drawbacks of powdered Perlite adsorbents by producing a durable monolithic architecture with excellent mechanical integrity, easy recovery, and good reusability. Furthermore, the well-ordered architecture may facilitate mass transfer by providing accessible diffusion pathways. The electrostatic interactions among 3D-printed polymer and MB can also contribute to the adsorption process and expand the role of 3D-printing beyond shaping the adsorbent.

Acid treatment also improves the surface properties and adsorption activity of 3D-Per15-A. The synergistic combination of these two approaches considerably enhances the practical applicability of the developed material for wastewater treatment.

Overall, this study introduces an efficient and environmentally friendly strategy for developing reusable monolithic adsorbents by integrating acid-modified natural Perlite with advanced DLP 3D-printing technology. The proposed fabrication route offers a cost-effective platform for producing robust adsorbents with high operational convenience and promising adsorption performance. Moreover, this strategy may be extended to the fabrication of other functional 3D-printed ceramic and mineral-based adsorbents for the removal of a broad range of emerging contaminants from water.

Conflict of interest

The author declares no conflict of interest.

Availability of data and materials

The data that support the findings of this study are available from the corresponding author, upon reasonable request.

Funding declaration

This work received no funding.

References

[1] C. Chatchiangkan, N. Azhari, T. Rojviroon, O. Rojviroon, F. Yalcinkaya, S. Pavasupree, J. Phys. Chem. Solids **213**, 113603 (2026)

[2] M.R. Bera, S. Ghosal, T.N. Ghosh, M. Nanda Goswami, D. Jana, J. Phys. Chem. Solids **212**, 113570 (2026)

[3] V.N.-N. Ngo, N.V. Pham, T.M. Ha, T.H.V. Luong, N.-H. Cao-Luu, T.Q.C. Nguyen, G.H. Dang, J. Phys. Chem. Solids **209**, 113265 (2026)

[4] G. Sriram, K. Dhanabalan, T.H. Oh, Inorg. Chem. Commun. **189**, 116719 (2026)

[5] H. Wang, S. Zhao, T. Su, F. Yin, G. Chen, D. Miao, Inorg. Chem. Commun. **192**, 117327 (2026)

[6] A. Bajiya, R. Bansal, M. Nemiwal, Inorg. Chem. Commun. **191**, 117161 (2026)

[7] M. Gokcan, D.D.E. Koyuncu, M. Okur, Res. Chem. Intermed. **50**, 4125 (2024)

[8] H.A. Tabti, A. Ammam, B. Guezzen, M. Boudinar, A. Kadeche, A. Ramdani, B. Doumi, A.N. Ech-Chergui, R.A. Boudia, M. Adjdir, Res. Chem. Intermed. **50**, 2793 (2024)

[9] D. Karadeniz, Z. Kalaycıoğlu, B. Özuğur-Uysal, F.B. Erim, Res. Chem. Intermed. **52**, 1095 (2026)

[10] M. Rafatullah, O. Sulaiman, R. Hashim, A. Ahmad, Journal of hazardous materials **177**, 70 (2010)

[11] P.O. Oladoye, T.O. Ajiboye, E.O. Omotola, O.J. Oyewola, Results in Engineering **16**, 100678 (2022)

[12] F.H. Azhar, Z. Harun, R. Hussin, S.A. Ibrahim, R.A.R. Ahmad, M.F. Shohur, Emerging Advances in Integrated Technology **3**, 37 (2022)

[13] J.B.B. Mougnol, S. Rathilal, Advances in Materials Science and Engineering **2024**, 5704096 (2024)

[14] H.N. Hamad, S. Idrus, Polymers **14**, 783 (2022)

[15] I.M. Lipatova, L.I. Makarova, A.A. Yusova, Chemosphere **212**, 1155 (2018)

[16] H. Es-Sahbany, M. El Hachimi, R. Hsissou, M. Belfaquir, K. Es-Sahbany, S. Nkhili, M. Loutfi, M. Elyoubi, Materials Today: Proceedings **45**, 7299 (2021)

[17] A. Bashir, L.A. Malik, S. Ahad, T. Manzoor, M.A. Bhat, G. Dar, A.H. Pandith, Environmental Chemistry Letters **17**, 729 (2019)

[18] S. Mondal, H. Ouni, M. Dhahbi, S. De, Journal of hazardous materials **229**, 381 (2012)

[19] J. Du, B. Zhang, J. Li, B. Lai, Chinese Chemical Letters **31**, 2575 (2020)

[20] C.F. Mhina, H.Y. Jung, J.K. Kim, Chemosphere **253**, 126728 (2020)

[21] X. Liu, S. Zhao, Q. Li, P. He, X. Duan, D. Jia, Y. Zhou, Journal of the American Ceramic Society **108**, e20377 (2025)

[22] D. Lan, H. Zhu, J. Zhang, S. Li, Q. Chen, C. Wang, T. Wu, M. Xu, Chemosphere **293**, 133464 (2022)

[23] A.H. Jawad, A.S. Abdulhameed, Surfaces and Interfaces **18**, 100422 (2020)

[24] D. Robati, B. Mirza, M. Rajabi, O. Moradi, I. Tyagi, S. Agarwal, V. Gupta, Chemical Engineering Journal **284**, 687 (2016)

[25] A. Chaturvedi, B.N. Rai, R.S. Singh, R.P. Jaiswal, Reviews in Chemical Engineering **38**, 617 (2022)

[26] Kusumlata, B. Ambade, A. Kumar, S. Gautam, Limnological Review **24**, 126 (2024)

[27] J. Lin, W. Ye, M. Xie, D.H. Seo, J. Luo, Y. Wan, B. Van der Bruggen, Nature Reviews Earth & Environment **4**, 785 (2023)

[28] R. Rashid, I. Shafiq, P. Akhter, M.J. Iqbal, M. Hussain, Environmental Science and Pollution Research **28**, 9050 (2021)

[29] M.S. Akhtar, S. Ali, W. Zaman, Molecules **29**, 4317 (2024)

[30] A. Lafdali, S. Khizar, S. Atlas, M. Raihane, F. Aziz, A. Elaissari, Emergent mater. **9**, 171 (2026)

[31] R.R. Phogole, P.P. Mpungose, L. Nyaba, M. Mnguni, P.N. Nomngongo, Emergent Mater. **8**, 8055 (2025)

[32] L. Wang, C. Shi, L. Pan, X. Zhang, J.-J. Zou, Nanoscale **12**, 4790 (2020)

[33] M.A. Islam, I. Ali, S.A. Karim, M.S.H. Firoz, A.-N. Chowdhury, D.W. Morton, M.J. Angove, Journal of Water Process Engineering **32**, 100911 (2019)

[34] Y. Ji, F. Xu, W. Wei, H. Gao, K. Zhang, G. Zhang, Y. Xu, P. Zhang, Journal of Solid State Chemistry **295**, 121917 (2021)

[35] A.M. Herrera-González, M. Caldera-Villalobos, A.-A. Peláez-Cid, Journal of Environmental Management **234**, 237 (2019)

[36] M. Davraz, M. Koru, A. Akdağ, Ş. Kılınçarslan, Y. Delikanlı, M. Çabuk, Construction and Building Materials **263**, 120674 (2020)

[37] A.T. Hubbard, Encyclopedia of surface and colloid science, CRC press, 2002.

[38] E. Kapeluszna, Ł. Kotwica, W. Pichór, W. Nocuń-Wczelik, Sustainable Materials and Technologies **24**, e00160 (2020)

[39] H. Xiong, K. Yuan, J. Xu, M. Wen, Cement and Concrete Composites **116**, 103900 (2021)

[40] S. Edebali, Journal of Nanomaterials **2015**, 697026 (2015)

[41] S. Son, P.-H. Jung, J. Park, D. Chae, D. Huh, M. Byun, S. Ju, H. Lee, Nanoscale **10**, 21696 (2018)

[42] S.F. Iftekar, A. Aabid, A. Amir, M. Baig, J. Polym. **15**, 2519 (2023)

[43] M.S. Syed, M. Rafeie, R. Henderson, D. Vandamme, M. Asadnia, M.E. Warkiani, Lab Chip **17**, 2459 (2017)

[44] T. Taher, A. Rianjanu, Sep. Purif. Technol. **403**, 138636 (2026)

[45] R. Chaudhary, P. Fabbri, E. Leoni, F. Mazzanti, R. Akbari, C. Antonini, Prog. Addit. Manuf. **8**, 331 (2023)

[46] X. Wang, J. Liu, Y. Zhang, P.M. Kristiansen, A. Islam, M. Gilchrist, N. Zhang, Virtual Phys. Prototyp. **18**, e2248101 (2023)

[47] J. Nam, M. Kim, Nano Converg. **11**, 45 (2024)

[48] B.W. Karuniawan, I.C. Chou, W. Macek, L. Beránek, C.-P. Jiang, M. Ramezani, Rapid Prototyp. J., (2026)

[49] L. Liu, J. Li, Y. Guo, Y. Wang, J. Dong, Z. Jiang, X. He, Rapid Prototyp. J., (2026)

[50] J. Zhang, C. Wang, J. Yang, Rapid Prototyp. J. **32**, 1975 (2026)

[51] A.L.T. Zheng, E.Y.L. Teo, O.F. Marzuki, L.F. Koo, T.J. Wong, E.L.T. Chung, Y. Andou, Eng. Res. Express **7**, 032001 (2025)

[52] F. Ranjbar, A.M. Rezadoust, S. Sadjadi, M. Atai, Prog. Addit. Manuf. **11**, 1317 (2026)

[53] A.M. Rezadoust, S. Sadjadi, A. Heydari, J. Mol. Struct. **1305**, 137808 (2024)

[54] S. Sadjadi, A.M. Rezadoust, S. Yaghoubi, E. Monflier, A. Heydari, ACS Omega **8**, 45844 (2023)

[55] C. Alparslan, Ş. Bayraktar, Polymers **17**, 1287 (2025)

[56] S. Hock, C. Rein, M. Rose, ChemCatChem **14**, e202101947 (2022)

[57] J. Lu, Y. Zhou, Y. Zhou, Crit. Rev. **53**, 1709 (2023)

[58] C. He, X. Hu, Ind. Eng. Chem. Res. **50**, 14070 (2011)

[59] M. Doğan, M. Alkan, A. Türkyilmaz, Y. Özdemir, J. Hazard. Mater. **109**, 141 (2004)

[60] M. Alkan, M. Doğan, J. Colloid. Interface Sci. **243**, 280 (2001)

[61] B. Bayat, J. Hazard. Mater. **95**, 251 (2002)

[62] M.R. Utami, K. Riyani, T. Setyaningtyas, Indones. J. Pure Appl. Chem. **6**, 9 (2023)

[63] T. Mathialagan, T. Viraraghavan, J. Hazard. Mater. **94**, 291 (2002)

[64] E. Ayranci, N. Hoda, Chemosphere **60**, 1600 (2005)

[65] M. Giannouri, T. Kalampaliki, N. Todorova, T. Giannakopoulou, N. Boukos, D. Petrakis, T. Vaimakis, C. Trapalis, INT J PHOTOENERGY **2013**, 729460 (2013)

Supplementary Files

This is a list of supplementary files associated with this preprint. Click to download.

- Supportinginformation.docx